Photocopy and Use Authorization

In presenting this thesis in partial fulfillment of the requirements for an advanced degree at Idaho State University, I agree that the Library shall make it freely available for inspection. I further state that permission for extensive copying of my thesis for scholarly purposes may be granted by the Dean of the Graduate School, Dean of my academic division, or by the University Librarian. It is understood that any copying or publication of this thesis for financial gain shall not be allowed without my written permission.

Signature ____________________________________

Date ____

A Landslide Inventory and Analysis

for Grand Teton National Park, Wyoming

by

Joshua D. Lingbloom

A thesis

submitted in partial fulfillment

of the requirements for the degree of

Master of Science in Geology

Idaho State University

Summer 2022

Committee Approval

To the Graduate Faculty:

The members of the committee appointed to examine the thesis of Joshua Lingbloom find it satisfactory and recommend that it be accepted.

Dr. Benjamin Crosby,
Major Advisor

Dr. Donna Delparte,
Committee Member

Dr. DeWayne Derryberry,
Graduate Faculty Representative

Acknowledgements

First and foremost, I would like to thank my advisor, Dr. Benjamin Crosby, for the tireless efforts of educating me on digital and field landslide mapping, reviewing my mapping and writing, and procuring much of my funding. I, likewise, extend my gratitude to my other committee members, Dr. Donna Delparte and Dr. DeWayne Derryberry, for lending me their expert knowledge on statistical analysis, and my assistant Daniel Vega, for making the summer 2021 field work possible. I would also like to thank the following individuals for their support: Simeon Caskey, Gus Smith, and Joni Gore with the Grand Teton National Park Service for their assistance through permitting (GRTE-2022-SCI-0005), providing data, and joining me in the field; Seth Wittke and James Mauch with the Wyoming State Geologic Survey for shared time in the field; Bill Burns with the Oregon Department of Geology and Mineral Industries for guidance on digital mapping; Kyla Grasso for providing me with her preliminary landslide inventory geodatabase; and both my parents and ISU colleague Kyra Bornong for reviewing my writing.

This research would not have been possible without generous funding from the Geological Society of America Graduate Student Research Grant Program (2021 awardee), the Tobacco Root Geological Society's Field Scholarship (2021), the Center for Ecological Research and Education's Research Grant (2021), and Idaho State University's Jeff Geslin Geosciences Research Endowment (2021).

Table of Contents

List of Figures

List of Tables

List of Frequently Used Abbreviations

Ga	Billions of years before present
Ma	Millions of years before present
ka	Thousands of years before present
kyr	Thousands of years
GTNP	Grand Teton National Park
LiDAR	Light Detection and Ranging
DEM	Digital Elevation Model
DTM	Digital Terrain Model

A Landslide Inventory and Analysis for Grand Teton National Park, Wyoming
Thesis Abstract—Idaho State University (2022)

Mass movements are a widespread and frequently destructive occurrence in high-relief landscapes including northwest Wyoming's Teton Range. Since critical human infrastructure often co-occurs within these landscapes, landslide inventory maps serve as foundational datasets for assessing hazards and risks posed by future events. Here we use a 2014 LiDAR elevation dataset to produce a novel landslide inventory geodatabase encompassing ~1040 mass movements throughout Grand Teton National Park. Our diverse inventory serves as the basis of a geostatistical investigation exploring the extent to which various topographic domains and substrate lithologies contribute to variations in landslide occurrence and type. We find that mass movements occur in unique topographic and lithologic settings, and that slope and lithology provide the strongest predictors of the spatial distribution of the different types. These statistical findings provide a foundation for future susceptibility analyses and advance our understanding of where and how mass movements occur in other landslide-prone regions.

Key Words**:** landslide, landslide inventory map, Grand Teton National Park, Wyoming, LiDAR, geomorphology, geostatistics, mass movement

Chapter 1: Introduction

1.1 Problem Statement

Mass movements play a critical role in landscape evolution and pose a serious hazard to human lives and infrastructure, especially in steep mountainous regions that experience seismicity and intense precipitation (Cendrero et al., 2006; Highland and Bobrowsky, 2008; Hong et al., 2007). Increasing urbanization in these mass movement-prone regions and the uncertain impacts of climate change emphasize the necessity of ongoing efforts to improve community preparedness and mitigate further losses (Crozier, 2010; Hong et al., 2007; Bishop, 2013). One way to address this challenge is using systematic observations of where and how past movements have most frequently occurred in an affected area to identify trends in topographic and geologic domains that are most susceptible to future events. By consulting landslide susceptibility models derived from these observations, officials can assess the hazard and risk posed to vulnerable communities or infrastructure and choose where to adopt the most effective mitigation measures (Bishop, 2013; Napieralski et al., 2013; Hong et al., 2007; Vandromme et al., 2020).

This study seeks to apply a statistical approach to assess where and how mass movements occur in mountainous, landslide-prone regions by addressing the following two questions: (1) to what extent is landslide-producing topography different from that of the encompassing region? (2) to what extent do different mass movement styles occur in unique topographic and/or geologic domains? Towards this end, we apply several geostatistical tests to a comprehensive landslide inventory map produced from a 2014 LiDAR (light detection and ranging)-derived bare earth digital elevation dataset encompassing Grand Teton National Park (GTNP) the John D. Rockefeller Memorial Parkway, and the National Elk Refuge. GTNP is an ideal location for this study because it is prone to landslides and has wide variations in both topography and lithology (Love et al., 1992; Butler, 2013). Furthermore, multiple intersecting predisposing factors, including recent deglaciation and high topographic relief, and triggering factors, such as extreme precipitation and seismicity along the active Teton fault, heighten the widespread occurrence of slope failures that pose potential risks to the 3-4 million annual park visitors (NPS, 2019; Vandromme et al., 2020). Although this study does not address the *hazard* (the probability that a given event will occur in a specific location within a particular time) and *risk* (harm to communities and infrastructure) posed by specific events (van Westen, 2013; Soeters and van Westen, 1995), it does provide a foundational set of products that will facilitate future work toward these goals.

1.2 Background

1.2.1 Defining Mass Movements

A mass movement is a general term describing the downslope movement of a mass of rock and/or soil under the force of gravity (Cruden and Varnes, 1996; Varnes, 1978). Various terms and phrases, including “landslide,” “slope movement,” and “slope failure,” are commonly used interchangeably with “mass movement” throughout the literature (Cruden and Varnes, 1996; Highland and Bobrowsky, 2008). For the purposes of this thesis, we will use “landslide” to refer to all types of mass movements. GTNP contains almost all types of movement which, thus, demand definition here.

1.2.2 Classifying Mass Movements

Although numerous classification systems have been proposed to distinguish between different mass movement styles, the Varnes (1978) system (Figure 1.1) has remained the most widely adopted landslide classification system in the English language (Hungr et al., 2014). Later updated by Cruden and Varnes (1996), this system defines 29 unique landslide types according to two criteria: the mode of transportation and the kind of material mobilized. Five primary types of movement are proposed: slides, falls, flows, topples, and spreads.

<u>Slides</u> are the downslope movement of earth materials along a discrete failure plane. The transported materials tend to start movement as a cohesive mass over a single surface of rupture or relatively thin zones of intense basal shear strain, and there tend to be few to no internal shear surfaces (Cruden and Varnes, 1996; Campbell, 1985). Slides are subdivided by translational and rotational motion.

<u>Translational Slides</u> typically shear along a relatively planar failure surface such as a bedding plane, fault, joint, contact, or other discontinuity. The displaced mass may disintegrate into multiple smaller units as velocity and/or travel distance increases (Campbell, 1985; Highland and Bobrowsky, 2008). Translational slides are also called block slides when the transported mass moves as a single unit and experiences little to no internal deformation (Varnes, 1978; Campbell, 1985).

<u>Rotational Slides</u> have an upwardly-concave failure surface and an axis of rotation parallel to the contour of the slope. Often occurring in homogenous materials, they are typically deeper-seated than translational slides, with near-vertical headscarps and upwardly-displaced toes. Rotational slides that have multiple curved failure planes are also called slumps (Cruden and Varnes, 1996; Highland and Bobrowsky, 2008).

<u>Flows</u> involve the downslope transportation of materials in which motion is distributed across multiple internal short-lived, closely spaced shear surfaces. Whereas slides maintain some degree of internal cohesion, flow movement resembles that of a viscous fluid due to the

substantial relative motion of particles within the moving mass (Varnes, 1978; Cruden and Varnes, 1996; Campbell, 1985). Flows are often described as “wet” or “dry” depending on if their interstitial pore fluid is air or water. For example, channelized debris flows are a common form of a rapid, wet flow in which a slurry of earth materials and water are channeled down steep gullies. Conversely, extremely rapid dry flows formed by the collapse and subsequent transport of materials on steep hillslopes are called avalanches (Cruden and Varnes, 1996; Hungr, 2007).

Falls describe the rapid vertical downward displacement that occurs when materials are detached from steep hillslopes. Transport occurs through free-falling, bouncing, or rolling, and there is little to no shear displacement (Campbell, 1985; Hungr, 2007).

Topples occur when a mass detaches from a steep hillslope and rotates forward away from the slope about an axis below the displaced mass’s center of gravity. Topples often occur within vertically-jointed bedrock (Campbell, 1985; Hungr, 2007).

Lateral spreads are flat to low-angle translational displacements that cause subsidence and lateral extension within a coherent mass following liquefaction or flow of a weaker underlying layer. This results in shear or tensile fractures within the overlying unit (Varnes, 1978; Campbell, 1985). Spreads are often triggered by seismic activity, and frequently occur along coastlines or artificial fill over former wetlands (Highland and Bobrowsky, 2008; Varnes, 1978).

A sixth category, complexes, describes cases in which a composite of two or more of the primary types are required to describe a movement (Hungr et al., 2014; Varnes, 1978).

The dominant type of material mobilized by each movement type is broadly divided into unweathered rock, intact prior to the initiation of movement and engineering soil. Engineering soil refers to any unconsolidated or poorly-cemented aggregate of rock fragments or particles, including weathered bedrock. Engineering soil is further divided into debris, where at least 20-80% of the fragments are coarser than 2 mm (sand size) and the remaining are 2 mm or finer, and earth where at least 80% of the particles are 2 mm or finer in size (Cruden and Varnes, 1996; Varnes, 1978; Campbell, 1985).

Later publications including Campbell (1985) and Hungr et al. (2014) sought to revise the Varnes (1978) classification system by incorporating modern geotechnical material definitions and nomenclature into additional landslide types and supplementary terms that more precisely describe the failure style and the material properties including the composition and moisture content. However, they will not be implemented here because we wish to maintain the greatest degree of compatibility with existing landslide inventories and susceptibility models, which continue to overwhelmingly adopt the taxonomy presented in Varnes (1978) and Cruden and Varnes (1996).

1.3 Landslide Inventories

1.3.1 Purpose

A key guiding principle for evaluating landslide hazards is that *the past is the key to the future* (Highland and Bobrowsky, 2008). In other words, the same topographic, geologic, and land cover conditions that contributed to a prior mass movement can lead to future slope failures of a similar nature. By recognizing patterns among the predisposing factors associated with the landslides present in an area, as well as identifying where past landslides have occurred, one can identify which locations are most susceptible to future landslides or reactivations of older movements. Based on this knowledge, one can further address the specific landslide hazards present at a given location and ultimately mitigate the potential risks posed to people and infrastructure (Napieralski et al., 2013; Vandromme et al., 2020; Galli et al., 2008).

Before analyzing landslide susceptibility or assessing local hazard and risk, it is essential to build a landslide inventory database. These are foundational datasets which seek to describe the distribution, extent, and characteristics of all mass movements within a given domain (Galli et al., 2008; Guzzetti et al., 2012; Vandromme et al., 2020). They can identify all movements present on the landscape or be limited to specific failure styles or a particular time interval. Likewise, their extent and level of detail can widely vary from local to regional depending on the area of interest and spatial resolution of the available data coverage (Guzzetti, et al., 2012).

1.3.2 Traditional Techniques

The variety of techniques available to prepare landslide inventories has grown with the emergence of new technologies. Geomorphological field mapping is the traditional approach to making landslide inventories (Guzzetti, 2012). Although this method allows workers to make detailed observations, rugged terrain limits the area that can be mapped and the spatial scope of inference. It can also be difficult to recognize the extent of large or heavily vegetated landslides. In recent years, GPS technology has offset some these limitations by enhancing the accuracy of data collected in the field (Guzzetti, 2012).

Visual interpretation of aerial imagery has remained the conventional tool for producing landslide inventories since airborne photographs became widely available in the 1930’s and 1940’s (Keefer, 2002; Guzzetti, 2012; Napieralski, 2013). This method is inexpensive and efficient, especially with the aid of stereoscopic viewers (Guzzetti, 2012). Since the 1970’s, the availability of multitemporal satellite imagery has enabled researchers to detect slope failures triggered by discrete precipitation or seismic events throughout an affected region (Napieralski, 2013). However, aerial imagery comes with several limitations. For example, the spatial resolution of the imagery limits the size of landslides that can be mapped, and heavy vegetative cover can increasingly obscure the boundaries of older failures. Although field observations can address some of these limitations, it often remains difficult to discern the type of movement and the boundaries of large or deep-seated landslide complexes, especially in inaccessible or vegetated environments (Keefer, 2002; Guzzetti, 2012).

1.3.3 Modern Techniques

Recent advances in geographic information system (GIS) software has allowed researchers to analyze topography using digital elevation models (DEMs). In particular, light detection and ranging (LiDAR) systems penetrate gaps in the forest canopy and reveal bare-earth topography with sub-meter spatial resolution, allowing researchers and state geologic surveys to develop landslide inventories with unprecedented efficiency, resolution, and accuracy (McKean and Roering, 2004; Napieralski, 2013; Bishop, 2013; Guzzetti et al., 2012). For example, a 2005 pilot project by the Oregon Department of Geology and Mineral Industries found that a LiDAR-assisted digital mapping approach allowed researchers to identify three to 200 times the number of landslides than inventories produced with aerial photographs or lower-resolution DEMs alone (Burns and Madin, 2009). Finally, interferometric synthetic aperture radar (InSAR) techniques can detect and monitor landslides by comparing multitemporal radar images collected from satellites to measure subtle ground surface deformation (Mondini et al., 2021; Napieralski, 2013).

1.3.4 Landslide Susceptibility

As second-order derivatives of landslide inventories, landslide susceptibility maps predict the likelihood of future mass movements occurring throughout a given domain (Reichenbach et al., 2018). Accurately performing these higher-order assessments requires a thorough understanding of the local conditions that influence where landslides occur in a given area. Reichenbach et al. (2018) notes that susceptibility studies may use a variety of techniques: (1) a statistical approach that employs methods such as regression (e.g., Erener and Düzgün, 2010) or machine learning (e.g., Crawford et al., 2020) to quantify the relationship between one or more instability factors and the distribution of landslides in a given domain, (2) a physically-based approach that uses numerical modeling and geotechnical investigations to analyze the driving and resisting factors controlling slope stability (e.g., Vandromme et al., 2020), (3) a qualitative heuristic approach in which factors assumed to drive instability are ranked and weighted by their relative influence on causing mass movements (e.g., Stevenson, 1977), or (4) a combination of approaches (e.g., Pellicani et al., 2013; Bălteanua et al., 2020). Moreover, a single susceptibility model can consider all mass movements en masse (e.g., Erener and Düzgün, 2010) or separate models can be prepared for specific movement styles (e.g., Boualla et al., 2019). Susceptibility models are often evaluated by their ability to fit the distribution of known landslides used to calibrate the model or their performance in predicting landslides not used to train the model (Reichenbach et al., 2018). Finally, susceptibility studies are the basis for higher-order hazard studies that assess the probability that a mass movement of a given magnitude and intensity will occur in a given location and period of time (van Westen, 2013; Reichenbach et al., 2018).

1.4 Study Area

1.4.1 Geologic Setting

Grand Teton National Park is located in northwestern Wyoming and encompasses the central and eastern flanks of the Teton Range and much of the adjacent Jackson Hole basin to the east (Figure 1.2). The park's complex geologic history is reflected by a diverse suite of bedrock lithologies, which are described extensively by Love et al. (1992) and are summarized by Love et al. (2003), KellerLynn (2010), and Henderson et al. (2020). The oldest rocks in the park consist of Archean gneiss, amphibolites, ultramafic rocks, and metagabbro. This suite of crystalline rocks underwent metamorphism in late Archean time at around 2.680 Ga and were subsequently intruded by the Mount Owen Quartz Monzonite around 2.547 Ga (Zartman and Reed, 1998). Finally, numerous subvertical diabase dikes intruded the Archean rocks in the Late Proterozoic around 769 Ma (Harlan et al., 1997). These Precambrian basement rocks are exposed in the eastern flanks of the central Teton Range, where they are weathered into steep sided canyons and a chain of prominent peaks that are the highest in the region.

A nonconformity separates the Precambrian rocks from the overlying Paleozoic sedimentary rocks. Deposition began in the Cambrian Period with the Flathead Sandstone around 510 Ma and continued through the Mesozoic Era with a sequence of interbedded fossiliferous shales, limestones, dolostones, and nearshore sandstones that reflect repeated transgressions and regressions of a shallow sea. In the Late Cretaceous period, the Cretaceous Interior Seaway deposited thick shales and sandstones that transitioned into terrestrial sandstones and conglomerates interbedded with coal as the seaway retreated and the Sevier orogeny uplifted highlands to the west. The Sevier orogeny continued into the Cenozoic era and was immediately followed by the Laramide orogeny. As these mountain-building events thrusted sheets of sedimentary strata upwards near the modern-day Teton Range, the Jackson Hole basin subsided to the east (Love et al., 1978). A thick package of sediments shed from the surrounding highlands filled this basin throughout the Paleogene and Neogene periods.

The Cenozoic era was also marked by volcanism, which emplaced extensive tuff, breccia, and other extrusive rocks throughout GTNP and the surrounding area. Regional volcanism initiated between 53-43 Ma with the eruption of the Absaroka volcanic field northeast of the park (Smedes and Prostka, 1972). Sediments from these eruptions are preserved on the eastern side of GTNP in the lacustrine deposits of the Colter and Shooting Iron Formations (Leopold et al., 2007). Next, eruptions from the Heise volcanic field in the eastern Snake River Plain deposited the Conant Creek Tuff and Kilgore Tuff throughout the park in 5.51 Ma and 4.45 Ma, respectively (Leopold et al., 2007; Morgan and McIntosh, 2005). Finally, the Yellowstone Plateau volcanic field began to erupt just north of the Park in 2.08 Ma (Rivera et al., 2014). Evidence of Yellowstone's ongoing hotspot volcanism is recorded in GTNP by the Teewinot Formation, Lewis Creek Rhyolite, and Lava Creek Tuff (Leopold et al., 2007; Shamloo and Till, 2019).

1.4.2 Tectonic Setting

The steep topography of the Teton Range is the product of both contractional and extensional tectonic regimes. An initial period of uplift occurred in the Late Cretaceous and early Paleogene periods when the Laramide Orogeny thrust Paleozoic and Mesozoic sedimentary strata eastward along the Buck Mountain fault (Love et al., 1978; KellerLynn, 2010; Love et al., 2003). Basin and Range crustal extension and regional tectonism associated with the Yellowstone hotspot triggered the rapid and ongoing uplift of the modern fault-block range along the Teton fault (White et al., 2009; Brown et al., 2017). This north-striking normal fault bounds the eastern flank of the range and extends at least 72 km from approximately 3 km south of Wilson to at least the northern boundary of GTNP (Figure 2.1; Zellman et al., 2019; Brown et al., 2017). An estimated 6 km of rapid vertical displacement along the fault (Brown et al., 2017) has resulted in the Teton Range's asymmetry characterized by gently sloping western slopes dominated by back-tilted Paleozoic sedimentary strata and steep eastern slopes composed of Precambrian crystalline basement rock (Figure 1.3; Love et al. 1992).

Thermochronologic modeling by Brown et al. (2017) suggests that the Teton Fault first initiated along the northern part of the Teton Range around 15-13 Ma before propagating to its present southern extent at 7 Ma. The late Cenozoic history of fault motion is also indicated by the tilting of volcanic and sedimentary rocks at Signal Mountain (Pierce et al., 2018). DuRoss et al. (2019) noted evidence of Holocene events on the southern Teton Fault at 9.9 ka, 7.1 ka, and 4.6 ka. This recent fault activity is manifested by fault scarps up to 30 m tall that offset Pinedale-age glacier deposits (Smith et al., 1993), and indicates significant Holocene seismic activity. It is believed that the fault is capable of generating a magnitude 7.5 earthquake today (White et al., 2009).

1.4.3 Glacial Record

Pleistocene climate fluctuations in the GTNP region resulted in many episodes of glaciation. However, the modern geomorphic record only preserves evidence of the past two glacial periods: the Bull Lake glaciation and the Pinedale glaciation (Foster et al., 2010; Pierce et al., 2018). The Bull Lake glaciation, which occurred from 190-130 ka, was the most extensive of the two (Pierce et al., 2018; Liccardi and Pierce, 2018). A lobe of ice advanced from the Yellowstone plateau to bury the Jackson Hole valley beneath approximately 700 m of ice (Pierce et al., 2018). Although the receding ice left extensive moraines, meltwater channels, scour features, and glacial erratics in the southern end of Jackson Hole, loess and outwash gravels from the subsequent Pinedale glaciation buried most of these features within GTNP (KellerLynn, 2010; Love et al., 1992).

The Pinedale glaciation occurred from 30-15 ka and was much less extensive than the Bull Lake glaciation (Pierce et al., 2018). During the Pinedale glaciation, mountain-valley glaciers sculped the Teton Range's characteristic landscape, including its deep glacial cirques, U-shaped valleys, and sharp horns and ridges (KellerLynn, 2010; Pierce et al., 2018). These glaciers extended to the western edge of Jackson Hole, where they deposited terminal moraines that today enclose several large lakes (Pierce et al., 2018). In addition, a far more massive ice stream advanced south from the Yellowstone Plateau ice cap and split into three lobes. These lobes were responsible for excavating Jackson Lake, scouring deep troughs, basins, and meltwater channels, and producing numerous glacial features including kettle lakes, eskers, and drumlins across the northern part of GTNP (Love et al., 1992, Pierce et al., 2018). Although the ice stopped short of Jackson Hole, its deep scouring generated a tremendous volume of cobbly gravel that buried the valley in broad glacial outwash fans up to 100 m thick (Love et al. 1992; Pierce et al., 2018).

The Teton Range experienced rapid deglaciation following the last glacial maximum (LGM). For example, cosmogenic ages of moraine boulders reveal that the deglaciation of Cascade Canyon (Figure 1.2) spanned a narrow 2.1 kyr window from 15.0-12.9 ka (Liccardi and Pierce, 2018). This is corroborated by the 13.8 ka onset of non-glacial sedimentation in Jenny Lake (Figure 1.2; Larsen et al., 2016) and a bedrock exposure age of 12 +/- 2 ka on the floor of Garnet Canyon (Figure 1.2; Tranel et al. 2015). However, Larsen et al. (2020) suggests that small remnants of glacial ice persisted as small debris-covered alpine glaciers or rock glaciers sustained by snow redistributed by wind and avalanching.

Analysis of alpine lake sediments reveals that glaciers in the Tetons began to readvance around 6.3 ka following a decline in summer insolation and a progressive shift to a cooler and wetter climate (Larsen et al., 2020). This glacial expansion culminated in two phases: one between 3.2-2.4 ka and a second, more extensive phase between 0.7-0.1 ka known as the Little Ice Age. These advances were separated by an interval of retreat caused by an extreme drought known as the Late Holocene Dry Period (Larsen et al., 2020; Larsen et al., 2016). All glaciers have retreated in the past century from their Little Ice Age limits and are expected to continue to retreat in response to anthropogenic climate change. Given sufficient insolating debris input and redistributed snow, glacial ice is expected to persist as debris-covered glaciers that may transition to stagnant rock glaciers (Larsen et al., 2020).

1.4.4 Paleoclimate History of the GTNP Region: LGM through the Present

Sediment records preserved in Yellowstone Lake (Brown et al., 2021), Jenny Lake (Larsen et al., 2016), and small alpine lakes (Larsen et al., 2020) offer insights into the paleoclimate and vegetation conditions experienced in GTNP and the greater Yellowstone region. The 14.7 ka Bølling Allerød warm period marked the onset of sustained warming following the LGM. Although this transition was briefly interrupted by the 13.5-11.5 ka Younger Dryas cooling event, by the early Holocene (9.88-6.7 ka) the regional climate was experiencing longer, hotter summers and greater aridity than present due to higher summer insolation and a strengthened northeastern Pacific subtropical high-pressure system. Winters were colder than the modern climate but experienced similar precipitation. The middle (6.7-3 ka) and late (3 ka-present) Holocene were marked by a shift to a progressively cooler and wetter climate with greater winter precipitation and colder summer temperatures. This coincided with an increase in forest density and large fire episodes. However, temporary shifts back to the warmer and drier conditions of the early Holocene did occur in 4.5-3 ka, 1.55-1.1 ka, and 1-0.7 ka.

The modern climate in GTNP is dominantly subarctic, and the lowest and highest elevations experience humid continental and tundra climates, respectively (Beck et al., 2018). The dry summer months are dominated by warm, moist air originating from the Pacific and Gulf of Mexico. Most precipitation is received as snow during the winter months, which are influenced by Arctic and Pacific air masses. The high topography of the Tetons and Yellowstone Plateau form an abrupt orographic barrier that captures moisture-laden Pacific Ocean air funneled east along the low-lying Snake River Plain. Consequently, annual precipitation increases with elevation (Licciardi and Pierce, 2018; Pierce et al., 2018; Foster et al., 2010).

1.4.5 Mass Movements in GTNP

Mass movements are a widespread occurrence throughout GTNP and the surrounding region due to numerous converging predisposing and triggering factors, including weak sedimentary dip slopes, glacially oversteepened and debuttressed canyon walls, frequent freeze-thaw cycles that accelerate mechanical weathering processes, intense summer precipitation that can rapidly oversaturate hillslopes, and active seismicity along the Teton Fault (Henderson et al., 2020; KellerLynn, 2010; Butler, 2013). Landslide dams are another regional concern, especially along major drainages. For example, the seismically-triggered 1925 Gros Ventre rockslide mobilized an estimated 38 million m^3 of rock to form a 69-76 m high dam on the Gros Ventre River east of GTNP that ultimately failed, creating a flood that killed 6 people downstream (Figure 1.2; Blackwelder, 1912; KellerLynn, 2010). The 1959 Hebgen Lake landslide, triggered by a 7.1 magnitude earthquake, dammed the Madison River northwest of Yellowstone National Park with an estimated 28 million m^3 of rock and formed a lake measuring 10 km in length and up to 58 m deep (Hadley, 1964). Twenty-eight people died as a consequence of the landslide and damming of the river.

Geochronological constraints for individual movements in GTNP are largely limited to rockfall/topple events. For example, a major rock topple that occurred in lower Cascade Canyon in late 2018 temporarily closed the popular Hidden Falls overlook (Huntington, 2018). In addition, Tranel and Strow (2017) analyzed cosmogenic ^{10}Be concentrations in talus fans to constrain the age of rockfall events in Garnet Canyon. The authors found that rockfall is an active process that has continuously occurred in the canyon following its 12-11 ka deglaciation and appears to be more closely linked to climate fluctuations, rather than discrete seismic events. Likewise, the 15-11 ka retreat of Pinedale ice constrains the maximum age of mass movement deposits preserved in GTNP. Debris originating from any mass movements that occurred prior to then would most likely have been transported and deposited in moraines or buried beneath the associated glacial outwash.

1.4.6 Previous Inventories

A limited number of studies have systematically addressed where and how mass movements occur throughout GTNP. Case (1990) used aerial photographs to map landslides across much of Wyoming in a series of 1:24,000 scale maps. A subsequent 1:62,500 scale geologic map of GTNP by Love et al. (1992) includes landslide debris among its Quaternary units. However, the authors did not subdivide the debris by landslide type.

More recent work by Butler (2013), Shroder and Weihs (2014), and Marston et al. (2011) incorporated detailed field observations, aerial imagery analysis, and GIS analysis of topographic datasets derived from ~10 m resolution DEMs to refine and expand Case's (1990) inventory. In addition, these studies performed the first local geostatistical analysis of landslides in GTNP to our knowledge in which descriptive statistics and chi-square tests identified which combinations of slope, aspect, rock strength, and other key variables control landslide style and frequency.

However, the mapping and interpretations were limited to five major canyons on the eastern flank of the range and only considered three styles of mass movement: rockfall, rock slides, and debris flows (Butler, 2013). Most recently, Mauch et al. (2021) published a 1:100,000 scale surficial geologic map of the western part of GTNP. Although this is the first study to use the parkwide LiDAR dataset, its utility as a landslide inventory is limited because of its coarse scale, focus on deposits, and undifferentiated styles of failure.

Our research builds upon these previous workers' efforts by using the superior mapping capabilities of LiDAR imaging to produce the first comprehensive landslide inventory map of GTNP at the much finer scale of 1:4,000. This enables us to address the gap in quantitative knowledge concerning how different topographic domains and geologic substrates contribute to landslide susceptibility throughout GTNP.

1.5 Thesis Structure

This thesis has three chapters. This introductory chapter details the background and motivation for our research. The second chapter is a standalone paper summarizing our research in a concise format intended for journal publication. It provides our methods, descriptions of the mapped units, and our statistical findings. The third and final chapter presents and interprets our findings while also emphasizing the implications of our work and opportunities for future research.

Chapter 1 Figures

TYPE OF MOVEMENT		TYPE OF MATERIAL		
		BEDROCK	ENGINEERING SOILS	
			Predominantly coarse	Predominantly fine
FALLS		Rock fall	Debris fall	Earth fall
TOPPLES		Rock topple	Debris topple	Earth topple
SLIDES	ROTATIONAL	Rock slide	Debris slide	Earth slide
	TRANSLATIONAL			
LATERAL SPREADS		Rock spread	Debris spread	Earth spread
FLOWS		Rock flow (deep creep)	Debris flow (soil creep)	Earth flow (soil creep)
COMPLEX		Combination of two or more principal types of movement		

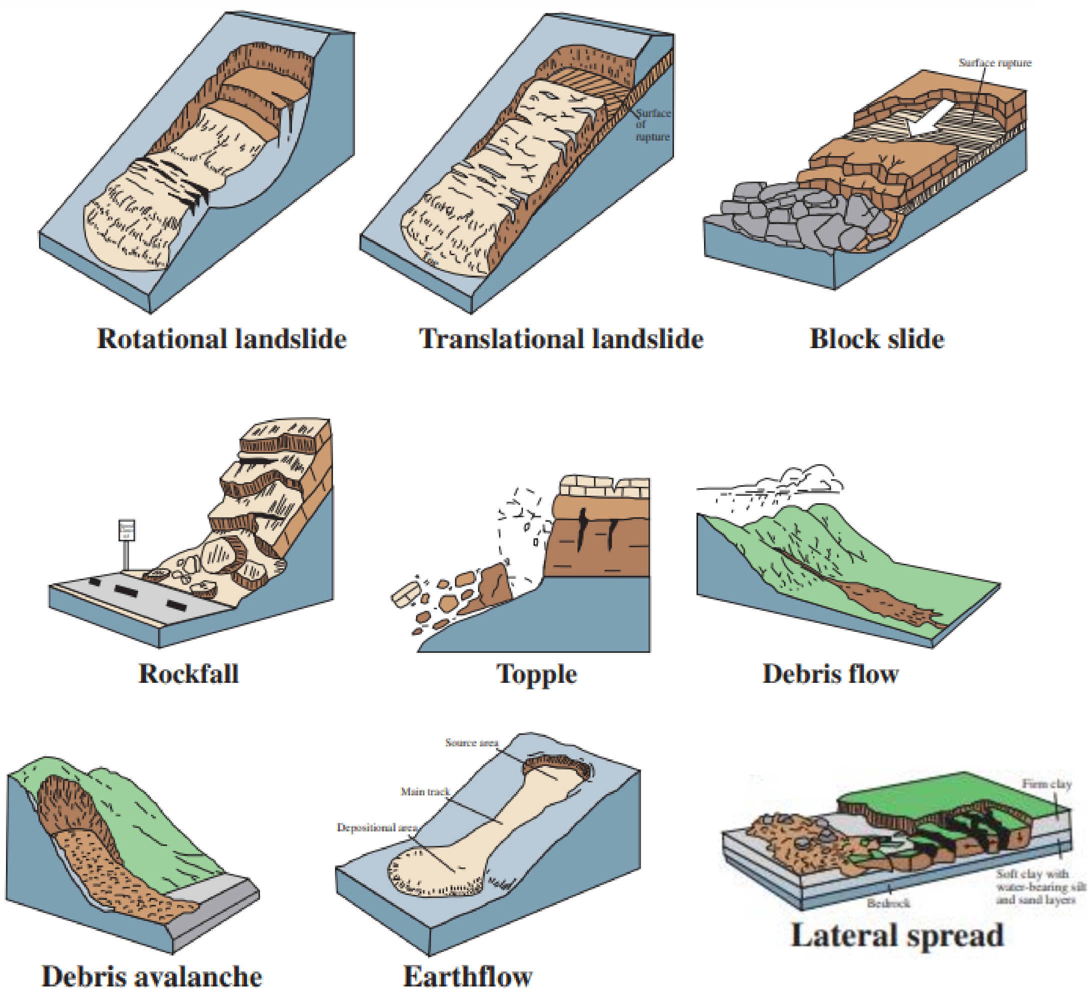

Figure 1.1: (top) The Varnes (1978) classification system distinguishes unique mass movement styles by type of movement and type of material involved. (center and bottom) Block diagrams of common mass movement styles modified from Highland (2006).

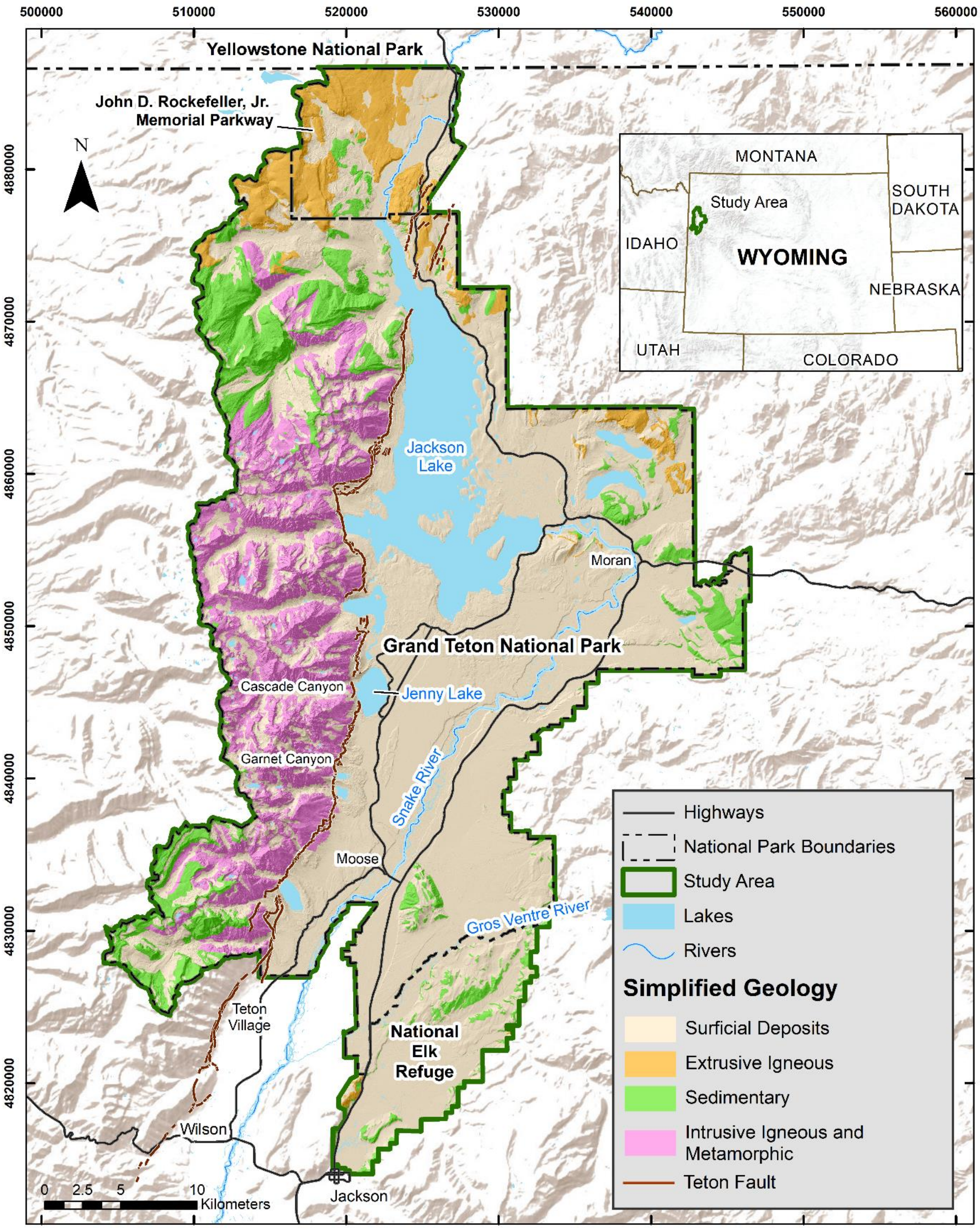

Figure 1.2: Map of the study area, which encompasses Grand Teton National Park and the John D. Rockefeller, Jr. Memorial Parkway. Solid green and grey dashed polygons outline the study area and park boundaries, respectively. The geologic units from which we will interpret the substrate lithology are simplified from Love et al. (1992). The measured grid is in NAD 1983 UTM Zone 12N. Hillshade basemap and transportation data courtesy of ESRI.

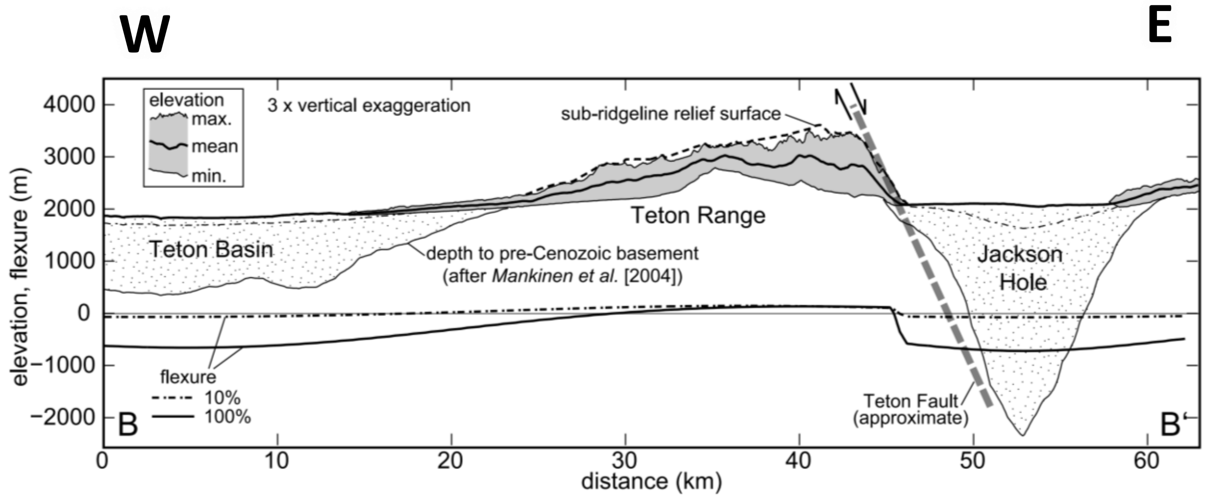

Figure 1.3: Schematic cross-section of the Teton Range highlighting the asymmetry between the gentle western (left) and steep eastern (right) flanks of the range. The Jackson Hole basin is the lightly shaded region east of the Teton Fault (heavy dashed line). Modified from Foster et al. (2010).

Chapter 2: A Landslide Inventory and Analysis for Grand Teton National Park, WY

Chapter 2 is formatted as a manuscript for submission to Earth System Science Data

2.1 Introduction

2.1.1 Objectives

Mass movements play a critical role in landscape evolution and pose a serious hazard to human lives and infrastructure, causing billions of US dollars in annual economic losses (Chung et al., 1995). Increasing urbanization in mass movement-prone regions and the uncertain impacts of climate change emphasize the necessity of ongoing efforts to improve community preparedness and mitigate further losses (Crozier, 2010; Hong et al., 2007; Bishop, 2013).

Ongoing research has addressed this challenge by observing where and how past movements have most frequently occurred in an affected area in order to predict the topographic and geologic domains that are most susceptible to future events. By consulting landslide susceptibility models derived from these observations, officials can assess the hazard and risk posed to vulnerable communities or infrastructure and choose where to adopt the most effective mitigation measures (Bishop, 2013; Napieralski et al., 2013; Hong et al., 2007; Vandromme et al., 2020).

This study applies a statistical approach to better understand where and how mass movements occur in the steep, landslide-prone topography of northwestern Wyoming’s Teton Range by addressing the following two questions: (1) to what extent is landslide-producing topography different from that of the encompassing region? (2) to what extent do different mass movement styles occur in unique topographic and/or geologic domains? Towards this end, we apply several geostatistical tests to a comprehensive landslide inventory map produced from a

2014 LiDAR (light detection and ranging)-derived bare earth digital topographic dataset encompassing Grand Teton National Park (GTNP) and the adjacent John D. Rockefeller Memorial Parkway and National Elk Refuge.

GTNP is an ideal location for this study because numerous intersecting predisposing factors, including glacially-oversteepened valleys and high topographic relief, and triggering factors, including extreme precipitation and seismicity along the active Teton Fault, heighten the widespread occurrence of slope failures that pose potential risks to the 3-4 million annual park visitors (NPS, 2019; KellerLynn, 2010). Furthermore, wide variations in both topography and lithology create a natural laboratory to observe how different topographic and geologic domains affect where and how movements occur. Although evaluating specific hazards (the probability that a given event will occur in a specific location within a particular time) and risks (harm to communities and infrastructure posed by specific events) is not within the scope of this study, the landslide inventory and statistical findings described here will serve as foundational products that facilitate future efforts to further these goals (e.g., van Westen, 2013; Soeters and van Westen, 1995)

2.1.2 Landslide Classification

A mass movement is a general term describing the downslope movement of a mass of rock and/or soil under the force of gravity (Cruden and Varnes, 1996; Varnes, 1978). Various terms and phrases, including "landslide," "slope movement," and "slope failure," are commonly used interchangeably with "mass movement" throughout the literature (Cruden and Varnes, 1996; Highland and Bobrowsky, 2008). Here the term "landslide" is used to refer to all types of mass movements.

Although numerous classification systems have been proposed to distinguish between different mass movement styles, the Varnes (1978) system (and its subsequent update by Cruden and Varnes (1996)) has remained the most widely adopted landslide classification system in the English language (Hungr et al., 2014), and is hence implemented in this study. This taxonomy defines 29 unique landslide styles according to two criteria: the mode of transportation and the type of materials mobilized. Landslides are divided into five primary styles of movement: slides, falls, flows, topples, and spreads. Slides are subdivided into translational and rotational slides by the curvature of the failure surface. A sixth category, complexes, describes cases in which a composite of two or more of the primary types are required to describe a movement (Cruden and Varnes. 1996; Varnes, 1978).

The dominant type of material mobilized by each movement type is broadly divided into unweathered rock, intact prior to the initiation of movement and engineering soil. Engineering soil refers to any unconsolidated or poorly-cemented aggregate of rock fragments or particles, including weathered bedrock. Engineering soil is further divided into debris, where at least 20-80% of the fragments are coarser than 2 mm (sand size) and the remaining are 2 mm or finer, and earth where at least 80% of the particles are 2 mm or finer in size (Cruden and Varnes, 1996; Campbell, 1985).

2.1.3 Landslide Inventory Maps

Landslide inventory maps are descriptive datasets which systematically document the distribution, extent, and characteristics of mass movements within a given domain (Galli et al., 2008; Guzzetti et al., 2012). They can identify all movements present on the landscape or be limited to specific failure styles or a particular time interval (Guzetti et al., 2012). In addition to providing a first order assessment of where landslide activity has occurred in the past, and where future reactivations may occur, they serve as the foundation for higher-order assessments of susceptibility, hazard, and risk by facilitating investigations into the conditions influencing where and how landslides have occurred on the landscape (Napieralski et al., 2013; Vandromme et al., 2020; Galli et al., 2008). As discussed by Guzzetti et al. (2012), a growing number of tools are available for landslide inventory mapping. Although geomorphological data mapping and aerial imagery interpretation have remained the most widely-implemented approaches, emerging technologies including LiDAR, interferometric synthetic aperture radar (InSAR), and geographic information system (GIS) software have allowed inventory maps to be produced with unprecedented efficiency, accuracy, and resolution (Napieralski et al., 2013; Bishop, 2013; Guzzetti et al., 2012; Mondini et al., 2021). In particular, LiDAR systems are extremely useful for mapping forested landscapes because they penetrate the forest canopy and visualize bare-earth topography with sub-metric spatial resolution (McKean and Roering, 2004).

2.1.4 Geologic Setting

Grand Teton National Park is located in northwestern Wyoming and encompasses the central and eastern flanks of the Teton Range and much of the adjacent Jackson Hole basin to the east (Figure 1.2). The park's complex geologic history is reflected by a diverse suite of bedrock lithologies, which are described extensively by Love et al. (1992) and are summarized by Love et al. (2003) and KellerLynn (2010), and Henderson et al. (2020). The oldest rocks in the park consist of late Archean gneiss, amphibolites, ultramafic rocks, and metagabbro that were metamorphosed around 2.680 Ga and were subsequently intruded by the Mount Owen Quartz Monzonite at 2.547 Ga (Zartman and Reed, 1998) and again by numerous subvertical diabase dikes around 769 Ma (Harlan et al., 1997). These Precambrian basement rocks are exposed on the eastern flanks of the central Teton Range (Figure 2.1). The Precambrian rocks are overlain by a sedimentary sequence of interbedded sandstone, limestone, dolostones, and shale that were deposited in the Cambrian through the Late Cretaceous periods and subsequently thrusted and folded during the Sevier and Laramide orogenies. This deformation triggered the subsidence of the Jackson Hole basin and further deposition of Cenozoic sedimentary units (Love et al., 1978). These sedimentary rocks are exposed on the northern and western flanks of the Teton Range and throughout the eastern half of the park (Figure 2.1). Regional volcanism initiating between 53-43 Ma with the eruption of the Absaroka volcanic field (Smedes and Prostka, 1972) and continuing through 631 ka with eruptions from the Heise and Yellowstone Plateau volcanic fields deposited tuff, breccia, rhyolite, and other extrusive rocks throughout the northern and eastern areas of the park (Figure 2.1; Leopold et al., 2007; Shamloo and Till, 2019).

The Tetons are a fault block range bounded on their eastern flank by the north-striking, east-dipping Teton Fault (Figure 2.1; Zellman et al., 2019). A product of Basin and Range crustal extension and regional tectonism associated with the Yellowstone hotspot, the Teton Fault first initiated along the northern part of the Teton Range around 15-13 Ma before propagating to its present southern extent at 7 Ma (Brown et al., 2017). An estimated 6 km of rapid vertical displacement along the fault has resulted in an asymmetrical form in which gently-sloping western flanks overlain with back-tilted sedimentary strata are contrasted by steep eastern flanks exposing Precambrian crystalline basement rock (Brown et al., 2017; Love et al. 1992). Active tectonism and associated seismicity has continued into the Holocene with known events recorded on the southern Teton Fault at 9.9 ka, 7.1 ka, and 4.6 ka (DuRoss et al., 2019). It is believed that the fault is capable of generating a magnitude 7.5 earthquake today (White et al., 2009).

Pleistocene climate fluctuations in the GTNP region drove many episodes of glacial advance and retreat. However, the modern geomorphic record only preserves evidence of the past two glacial advances. The first and most extensive was the Bull Lake glaciation, which occurred from 190-130 ka, and at its maximum extent, buried the Jackson Hole valley beneath approximately 700 m of ice (Liccardi and Pierce, 2018; Pierce et al., 2018; Foster et al., 2010). During the subsequent Pinedale glaciation, which lasted from 30-15 ka, local valley glaciers sculped the Teton Range's characteristic U-shaped valleys and deposited extensive terminal moraines that today enclose several large lakes. In addition, the southern lobe of the Yellowstone Plateau ice cap excavated Jackson Lake and buried the Jackson Hole valley beneath glacial outwash fans up to 100 m thick (Love et al. 1992; Pierce et al., 2018).

The Teton Range experienced rapid deglaciation following the 15 ka Pinedale glacial maximum, with cosmogenic ages from Liccardi and Pierce, (2018), Tranel et al. (2015), and Larsen et al. (2016) suggesting that the range was nearly deglaciated by 11.5 ka. This age is notable because it constrains the maximum age of most mass movements observed throughout GTNP. Debris originating from any mass movements that occurred prior to then was most likely transported and deposited in moraines or buried beneath the associated glacial outwash. Remnants of several alpine glaciers continue to persist in the high parts of the Teton Range, having briefly advanced from 3.2-2.4 ka and again during the Little Ice Age from 0.7-0.1 ka. These glaciers owe their survival to the deep annual orographic snowfall generated as moisture-laden Pacific Ocean air is funneled east across the low-lying Snake River Plain until encountering this abrupt topographic barrier (Larsen et al., 2020; Licciardi and Pierce, 2018; Pierce et al., 2018; Foster et al., 2010).

2.1.5 Previous Landslide Inventories

Mass movements in GTNP and the surrounding region have been a focus of several studies. Case (1990) used aerial photographs to map landslides across much of Wyoming in a series of 1:24,000 scale maps. A subsequent 1:62,500 scale geologic map of GTNP by Love et al. (1992) includes undivided landslide debris among its Quaternary units. More recent work by Butler (2013), Shroder and Weihs (2014) and Marston et al. (2011) used field observations, aerial imagery, a ~10 m resolution digital elevation model (DEM) to refine Case's (1990) inventory and identify which combinations of topographic and geologic variables control landslide style and frequency in five major canyons on the southeastern flank of the Teton Range. Most recently, Mauch et al. (2021) used the LiDAR elevation dataset to create a 1:100,000 scale surficial geologic map of the western part of GTNP, which included undivided landslide deposits among its mapped units.

This study builds upon these previous workers' efforts by using the superior mapping capabilities of LiDAR imaging to produce the first comprehensive landslide inventory map of GTNP at the much finer scale of 1:4,000. This will help close the gap in quantitative knowledge concerning how different topographic domains and geologic substrates contribute to landslide susceptibility throughout GTNP.

2.2 Methods

2.2.1 Digital Mapping

All mass movement features in the study area were mapped at 1:4000 scale following the Burns and Madin (2009) protocol for LiDAR-aided landslide inventory mapping and classified following Cruden and Varnes (1996). Mass movement features were primarily interpreted from a 0.5 m resolution slope layer generated from a bare earth digital terrain model (DTM). The DTM was derived from a parkwide LiDAR dataset collected in summer 2014 with a pulse spacing of 0.7 m and a point density of 5.72 points/m^2 (Woolpert, 2014). To map the boundaries of movements partially extending beyond the GTNP LiDAR extent, we referenced 2019 NAIP aerial imagery and slope layers derived from a 10 m USGS DEM and a 0.5 m LiDAR-derived DTM encompassing Yellowstone National Park and part of the Bridger-Teton National Forest. Digitized copies of Case's (1990) landslide inventory map, the Mauch et al. (2021) surficial geologic map of the Jackson Lake quadrangle, and Butler's (2013) landslide inventory were also consulted during mapping.

Our inventory does not differentiate the age of the mass movements, but is rather a cumulative inventory of all movements that are detectable at a 1:4,000 scale as of the 2014 acquisition of the LiDAR dataset. These movements document the legacy of the past ~15 ka of mass wasting following the LGM.

2.2.2 Field Validation

Field investigations were conducted in the summers of 2020 and 2021 to validate the boundaries and classifications of a subset of the office-mapped mass movements throughout the study area. We also refined our inventory by removing features that we incorrectly interpreted as landslides, such as alluvial fans and moraines, and adding landslides that were not already mapped. Evidence of recent activity including tension cracks, hummocks, internal scarps, sag ponds, swales, and pistol-butted trees were also documented following Slaughter et al. (2017). The lithology in which the movements initiated was also identified by observing the bedrock units exposed in head scarps and clasts entrained within the deposits. Observations and feature class edits were recorded with ESRI's ArcGIS Field Maps mobile application. These validations increase quality of the landslide inventory map and geostatistical analysis.

2.2.3 Topographic and Geologic Attributes

To identify patterns in where and how landslides occur in GTNP, we first derived seven topographic or lithologic characteristics for each mapped movement. Although there is no agreement in the literature on which variables should be used for susceptibility analyses (Nefeslioglu et al., 2009), these attributes were selected because they are widely evaluated predisposing factors in landslide susceptibility studies (Reichenback et al, 2018) and were available in our study area. Although elevation, annual precipitation, vegetation density, and land cover are also commonly used in landslide susceptibility studies (Reichenback et al, 2018), we chose to omit them from this study because they are closely linked to climate, which has fluctuated greatly in GTNP since the LGM (Larsen et al., 2016). Since the movements recorded in this inventory occurred throughout the Holocene, we cannot assume that they initiated under the present-day climate and vegetation regime.

<u>Substrate lithology</u> describes the basal unit in which a mass movement was mobilized. All units from the 1:62,500 scale GTNP geologic map by Love et al. (1992) were aggregated into four classes: sedimentary rocks, intrusive igneous and metamorphic rocks, extrusive igneous rocks, and surficial deposits (Figure 2.1). These classes were defined by similar rock types and rheology generally following Bălteanua et al. (2020). Intrusive igneous and metamorphic rocks were grouped because they largely co-occur throughout the study area and share common discontinuities. Shallow slope failures that occurred in alluvium, terrace deposits, preexisting landslide deposits, or glacial till were assigned a surficial substrate lithology. Deep-seated movements that mobilized intact bedrock and shallow failures that scoured down to bedrock were assigned a non-surficial substrate lithology. This includes channelized debris flows that initiated in scoured bedrock channels and earth flows that failed along the interface of the

regolith and underlying unweathered bedrock. If the bedrock unit was concealed beneath surficial deposits, it was interpolated from the mapped bedrock unit nearest to the upper bounding scarp. These interpretations were confirmed and refined by field observations that identified the substrate lithology by examining exposures in the head scarp and/or fragments of transported bedrock within the body of the deposit. Finally, each channelized debris flow was assigned the lithology that encompasses the majority of its path since debris flows derive most of their volume by accumulating loose material along the length of the channel (Hungr, 2007).

Slope refers to the maximum rate of elevation change relative to horizontal. It has been widely cited in the literature as the strongest control on mass movement susceptibility because it directly affects the shear stress imparted on hillslope materials (Reichenback et al, 2018; Brardinoni et al., 2003; Campbell, 1985; Yilmaz et al., 2012). Slope was measured in degrees with the Add Surface Information tool, which interpolates elevation values at each of a polyline's vertices from a DEM and calculates their average slope using their difference in elevation and the 3D length along the elevation surface connecting them. The slopes of individual polyline segments are averaged by weighting them by their 3D lengths (ESRI, 2022a). The line segments were hand drawn on unfailed adjacent slopes, parallel to the downslope direction of the landslide, interpreted to be representative of the pre-failure topography (Figure 2.2). For rockfall and topple, slope was measured from the source area immediately upslope from the deposit. We measured the slope of channelized debris flows from the transport paths bounded by their initiation points and the top of each deposit.

Aspect describes the compass direction of maximum slope. It has been found to control the amount of solar insulation, drying winds, and moisture received by Teton hillslopes (Foster et al., 2010). These variables affect the rates of chemical weathering by moisture and temperature fluctuations and the mechanical weathering processes controlled by freeze-thaw cycles that predispose hillslopes to failure (e.g., Sahin et al. 2017; Ferrier et al., 2012; Yilmaz et al., 2012). We reported mass movement aspect as a generalized movement direction measured as an azimuth in degrees clockwise from north following Burns and Madin (2009). This was measured with line segments constructed from the center of each movement's head scarp/initiation point to the center of its toe.

The median aspect was calculated with equation 1 following Hodgson and Gaile (1996) where *asp rad* is each aspect in radians. This eliminates the problem inherent to a circular scale wherein taking a simple average of 350 degrees and 10 degrees would incorrectly yield a directional mean of 180 degrees. The directional variance was calculated by modifying equation 1 to take the interquartile ranges of cos(*asp rad*) and sin(*asp rad*).

Equation 1: $$\text{directional median} = \tan^{-1}\left(\frac{median(\cos(asp\ rad))}{median(\sin(asp\ rad))}\right) \times \frac{180}{\pi}$$

<u>Local vertical relief</u> is the maximum difference in elevation within a given distance of a point. Tectonic and glacial processes have imparted a strong contrast in local relief between the western and eastern sides of GTNP (Figure 2.3), providing an opportunity to observe how this variable affects slope failure style and distribution. Relief was calculated from the DEM by differencing the maximum and minimum elevations within a 1500 m radius circular moving observation window. The 1500 m radius was chosen to reflect the magnitude of upslope terrain contributing to a given deposit. In particular, 3000 m is the approximate length of the longest continuous hillslope contributing to any of the mapped deposits.

<u>Plan</u> and <u>profile curvature</u> describe the rate of change of slope perpendicular and parallel to the maximum slope direction, respectively (Nefeslioglu et al., 2008; Yilmaz et al., 2012). As

discussed by Minár et al. (2020), the magnitude of their values (measured in m/100) corresponds with the tightness of a slope's concavity or convexity (Figure 2.3). Positive plan curvature values indicate that the surface is upwardly convex while negative values indicate upward concavity. Conversely, negative profile curvature values correspond with upward convexity while positive values indicate upward concavity. Planar surfaces have plan and profile curvature values of zero. Both attributes were derived with the ArcGIS Curvature tool. Although there are numerous other approaches to calculating curvature such as the "standard curvature" that is a mean of plan and profile curvature (Minár et al., 2020), we chose to consider them separately (1) to ensure the greatest comparability with previous studies (e.g., Sahin et al., 2017; Crawford et al., 2020; Nefeslioglu et al., 2008) and (2) because they control different aspects of landslide kinematics. For example, plan curvature influences the convergence and divergence of surface and groundwater flow whereas profile curvature influences the acceleration and deceleration of downslope flow—and by extension its erosive capacity (Reichenback et al, 2018; Nefeslioglu et al., 2008; Yilmaz et al., 2012).

Topographic surface roughness broadly describes the variability of topography at a given scale (Grohmann et al., 2011). Although surface roughness has been proposed as a strong indicator of landslide susceptibility (Reichenback et al, 2018; Regmi and Walter, 2020), as a tool for automated landslide mapping (Bunn et al., 2019), and a tool for relative landslide age dating (Nicholas, 2018), there is no standard approach to quantifying it (Grohmann et al., 2011). Simple approaches that use a single topographic parameter (such as the standard deviation of elevation, slope, or profile curvature) have been proposed in the literature (Reichenback et al, 2018; Grohmann et al., 2011), as have more complex methods that derive a terrain ruggedness index (Moreno et al., 2003) or integrate multiple topographic parameters (Regmi et al., 2013). We calculated surface roughness (in degrees) by taking the standard deviation of slope from a moving observation window because of its simplicity of calculation and reliable performance in previous studies (Grohmann et al., 2011; Regmi and Walter, 2020; Nicholas, 2018). Regmi et al. (2013) notes that the size of the observation window should reflect the wavelength, or spatial frequency, of the topographic irregularities one wishes to capture. Because we are primarily interested in detecting the hummocky topography characteristic of landslide deposits, we chose a 10 m radius circular smoothing window to closely match the ~20 m spacing of hummocks observed in the study area. We frequently noticed circular artifacts in the output raster surrounding isolated boulders and scarps (Figure 2.3), which Crawford et al. (2021) suggests are a consequence of using a circular window to generate the roughness layer. The slope raster from which roughness was derived was generated with the Slope tool, which uses a DEM to calculate the rate of change in the x and y directions of a 3x3 cell moving observation window. This rate of change is converted to degrees and assigned to the central cell. This algorithm is described in detail by ESRI (2022b).

In order to eliminate surface irregularities and artifacts caused by interpolating LiDAR ground points that would otherwise add noise to the dataset and mask larger topographic trends in the slope's curvature and topographic surface roughness, the 0.5 m GTNP DTM was smoothed by calculating the mean elevation value within a 15 m radius circular moving observation window following Crawford et al. (2021). Shi et al. (2007) notes that although square smoothing windows are traditionally used for focal statistics, circular windows are more accurate when there is a high window to cell size ratio because they eliminate directional bias in the diagonal dimensions. Given the fine spatial resolution of the GTNP DTM, we chose to use circular windows for all focal statistics operations in this study.

As with the slope measurements, our approach to calculating vertical relief, curvature, and roughness varied by movement style (Figure 2.2). Thirty-meter radius buffers were constructed around points positioned near the center of each rockfall/topple source area and clipped to the source area boundaries. Buffering the points ensured that the measurements were not biased by small topographic variations. In addition, 10 m radius buffers were constructed around the channelized debris flow initiation points. This buffer radius corresponds to the ~20 m gully width observed at most of the initiation points. For all other movement types, 30 m radius buffers were constructed around points positioned on slopes adjacent to the disturbed area interpreted to reflect the terrain conditions prior to failure. The Zonal Statistics tool calculated the mean relief, curvature, and roughness within each buffer. Finally, the Yellowstone 0.5 m DTM and the USGS 10 m DEM were used to extract the topographic variables where movements extended beyond the GTNP DTM.

2.2.4 Geostatistical Analysis

Geostatistical analysis was performed to (1) compare the characteristics of landslide-producing topography to those of the bulk study area and (2) compare the characteristics of different mass movement styles. In order to decrease the size disparity between groups, movements were aggregated into four categories: rockfall/topple, debris flows, earth flows, and slides (Figure 2.4). Open-slope debris flows and channelized debris flows were grouped into a single category, as were translational and rotational slides. Complexes were reclassified by primary movement style. Topple was grouped with rockfall because it was not observed in unique settings. Because a large portion of GTNP encompasses low-gradient domains completely devoid of observed mass movements, we chose to exclude all lakes, glacial outwash plains, and rivers and their associated floodplain and fluvial terrace treads from our analysis of the bulk study area (Figure 2.3). Due to limited computational power, slope, aspect, relief, plan and profile curvature, and roughness datasets derived from the smoothed 0.5 m GTNP DTM were resampled to 5 m resolution before being exported as comma separated value (CSV) files.

Two statistical tests were implemented to identify whether clustering is present in the data. First, the average nearest neighbor test was performed within ArcGIS Pro to determine whether mass movements are evenly distributed throughout GTNP. As described by Clark and Evans (1954) and presented in equation 2, the average nearest neighbor ratio (ANN) was calculated by dividing the observed mean distance between each mass movement centroid and its nearest neighbor (D_o) by the hypothetical mean distance to nearest neighbor expected if all movements were randomly distributed throughout GTNP (D_e). If ANN is less than 1.0, then there is a clustering pattern in the data. If ANN is greater than 1.0, then there is a pattern of dispersion.

Equation 2: $$ANN = \frac{\mathrm{Do}}{\mathrm{De}}$$

Second, Syrjala's test of spatial independence between populations was performed in the R environment to assess whether the four movement styles occur in unique locations within GTNP. This nonparametric test compares the spatial distribution of two populations by comparing cumulative distribution functions constructed at each sampling location (Syrjala, 1996). The distributions are normalized to eliminate any biases from different sample counts between groups. Since the test requires all values to be sampled at the same set of locations, the four movement styles were compared using the cells of four overlapping kernel density layers generated for the entire study area. If Syrjala's test produced a large p-value (0.1 or more) for a given comparison, then the data is consistent with the null hypothesis that the two styles' spatial distributions are the same. If the test produced a small p-value (0.01 or less) we concluded that the data supports the alternative hypothesis that the two movement styles are differently distributed across the study area.

The remaining statistical tests were performed in the MATLAB environment. First, the two-sample Kolmogorov-Smirnov (K-S) test was used to individually compare the slope, aspect, topographic roughness, plan and profile curvature, and vertical relief of all mass movements with that of the bulk study area. This test assesses the degree to which two random sample distributions have been drawn from the same underlying distribution (Goodman, 1954), and has been used in previous studies to compare the attributes of different landslide inventories (Bellugi et al., 2021) and determine the degree of association between various topographic domains and failure styles (Irigaray and Fernández, 1996). If the K-S test produced a large p-value (0.1 or more), then the data is consistent with the null hypothesis that for a given topographic attribute, landslide-producing topography is not different from that of the bulk study area. If the test produced a small p-value (0.01 or less) we concluded that the data supports the alternative hypothesis that that characteristic of landslide-producing topography is different than that of the bulk study area.

Next, the Kruskal-Wallis test was used to individually test whether the four movement styles' slope, aspect, topographic roughness, plan and profile curvature, and vertical relief values originated from the same population. This non-parametric equivalent of the one-way ANOVA (analysis of variance) test is used to compare three or more groups within a categorical independent variable based on each group's mean rank of data values within a quantitative dependent variable (Kruskal and Wallis, 1952; Dai, 2018), and has been used to compare land use with landslide density and volume (Brardinoni et al., 2003). It was chosen because none of the six topographic variables satisfied ANOVA's assumption that that the dependent variable is both normally distributed and has an equal variance within each category. Although the ANOVA test has been widely used to compare landslide attributes (e.g., Carrara et al., 1982; Keefer, 2000), we suggest that the Kruskal-Wallis is a more statistically-sound alternative when the data did not satisfy its assumptions. These assumptions were tested with the Shapiro-Wilk test of normality and Levene's test of equal variance following Kim (2017). Since both tests produced small p-values for all topographic variables compared (Appendix 1), the data is consistent with the tests' alternative hypotheses that the four movement styles are not normally distributed and do not have an equal variance among each topographic variable. If the Kruskal-Wallis test produced a large p-value (0.1 or more) for a given topographic variable, then the data is consistent with the null hypothesis that that variable does not influence the style of failure. If the test produced a small p-value (0.01 or less) we concluded that the data supports the alternative hypothesis that at least one of the failure styles is different than the others based on that variable.

As seen in equation 3, the coefficient of determination (R^2) of each Kruskal-Wallis test was calculated for each topographic variable following Palacios-González and García-Fernández (2012), where the variance between each group (Model SS) was divided by the total variance in all observations (Total SS). This value describes the portion of the total variance within each variable that can be explained by separate populations.

$$\text{Equation 3:} \qquad R^2 = \frac{Model\ SS}{Total\ SS}$$

Because the Kruskal-Wallis test does not identify which combinations of movement types differ for a given topographic variable, we performed Dunn's multiple comparison test. This non-parametric post-hoc test makes pairwise comparisons of ranked values to determine which pairs of movement differ (Dunn, 1964). If Dunn's test produced a large p-value (0.1 or more) for a given comparison, then the data is consistent with the null hypothesis that that those two movement styles cannot be differentiated based on that topographic variable. If the test produced a small p-value (0.01 or less) we concluded that the data supports the alternative hypothesis that those two movement styles can be differentiated based on that variable.

Finally, we performed the chi-square test to compare the overall distribution of mass movement substrate lithologies with that observed throughout the park as well as that of each mass movement style. Commonly used in landslide statistical analysis to determine whether slope failures occur in unique geomorphic domains (e.g., Gritzner et al., 2001; Sahin et al., 2017; Butler, 2013), the chi-square test assesses the strength of association between each explanatory variable and each landslide type by comparing the actual number of movements observed in each category to the expected number of movements based off the overall distribution of each category across the entire dataset (van Westen, 1993; Rogerson, 2015; Sahin et al., 2017). If the chi-square test produced a large p-value (0.1 or more) for a given comparison, then the data is consistent with the null hypothesis that that substrate lithology does not affect where or how landslides occur in GTNP. If the test produced a small p-value (0.01 or less) we concluded that the data supports the alternative hypothesis that certain lithologies must be affecting the presence of mass movements or the failure style.

2.3 Results

2.3.1 Landslide Inventory

A total of 1040 unique mass movements were mapped in the park along with 12 suspected movements and 34 rock glaciers. The mass movement deposits have a combined surface area of 76.1 km^2, or 5.2% of the study area. The movements have a non-uniform spatial distribution, with the highest concentrations found in the steep high-relief topography west of the

Teton Fault and a lower frequency in the flatter, lower-relief terrain east of the Teton Fault (Figure 2.4). The distribution of movement styles is likewise heterogeneous, with channelized debris flows (42% of population), earth flows (24%), and rockfall (17%) occurring with the greatest abundance.

2.3.2 Description of Mapped Units

The following unit descriptions explain how each movement style was recognized and mapped. This includes (1) techniques for distinguishing mapped units based on their diagnostic features and (2) interpretations of the settings in which they occur derived from field observations. The statistical exploration of these observations is tested in sections 2.3.3 and 2.3.4.

2.3.2.1 Slides

Each slide is defined by a polygon encompassing the mobilized mass, a polygon encompassing the upper bounding scarp exposed where the mass detached from the stable hillslope, and polylines tracing the upper edges of internal scarps and/or tension cracks, if applicable. Few slides remain coherent blocks, but rather disaggregate into earth flow complexes. Three styles of slides are observed:

Translational rock slides (RS-T; Figure 2.3) are found on weak sedimentary and extrusive dip slopes. They typically have linear headscarps and lateral bounding scarps. Linear internal scarps and tension cracks intersect the deposits perpendicular to the transport direction. Tension cracks are sometimes present immediately upslope of the head scarp. Depending on the transport distance and velocity, the deposits vary from undeformed, cohesive blocks to hummocky, bouldery masses.

Rotational rock slides (RS-R; Figure 2.3) are observed on jointed sedimentary and extrusive anti-dip slopes. They are characterized by massive back-rotated blocks with near-vertical, cusp-shaped headscarps and upwardly-displaced toes that are more pronounced than those of translational slides. Multiple nested cusp-shaped internal scarps from successive failures are frequently observed in the deposits. This internal displacement tends to disrupt the internal drainage and form sag ponds or depressions throughout the deposit.

Rotational earth slides (ES-R) are found on homogeneous surficial deposits such as glacial till, soil, and alluvium, and are often found along cutbanks of fluvial channels. They resemble rotational rock slides but tend to be smaller, shallower, and more localized.

2.3.2.2 Flows

Three styles of flows are observed in GTNP. Earth flows (EFL; Figure 2.3) are commonly found on forested, moderately-steep, soil mantled hillslopes, especially where weak sedimentary or extrusive units are present. They initiate on the contact between the regolith and the underlying bedrock, and have steep cusp-shaped headscarps that are shallower than those of rotational rock slides. The hummocky deposits typically have multiple overriding lobes and a high water table that supports dense deciduous vegetation. The internal deformation that distinguishes flows from slides is often manifested by compressional ridges that are oriented transverse to the flow direction and enclose closed basins, as well as elongated levees that parallel the direction of downslope movement (Coe et al., 2009). Seeps are commonly observed along the base of the lobate toes. Each earth flow is mapped by a polygon enclosing the mobilized mass, a polygon encompassing the upper bounding scarp, and polylines tracing the head of internal scarps where reactivation has occurred. If distinct reactivated features were visible the 1:4,000 scale, they were mapped as separate deposits.

Channelized debris flows (DFL-C; Figure 2.3) are confined to pre-existing channels or gullies and have specific domains of material scouring/transport and deposition. Each channelized debris flow was mapped following Burns and Madin (2009) with an initiation point, a transport path polyline, and a polygon enclosing the deposit. Debris flows are interpreted to initiate on the uppermost point along the channel that scouring is observed. Upstream of this point, the channel is either indistinct or intersects a low-gradient hanging valley or ridgeline. Debris flow paths tend to follow steep, constricted bedrock channels. If multiple tributaries contributed material, the debris flow path was mapped following the most distinct channel, which was interpreted to be the most recently active. The deposits are typically fan-shaped and encompass the area of deposition. They are unsorted, matrix supported, and composed of boulder to pebble sized rocks, soil, and dead vegetation. Fans typically have multiple active and abandoned channels bounded by natural levees comprised of coarse material.

Open-slope debris flows (DFL-O) are distinguished from channelized debris flows following Cruden and Varnes (1996), where the movement forms its own path down a hillslope, rather than being confined to an existing channel. Open-slope debris flows are hummocky, lobate deposits that resemble earth flows, but mobilize coarser material such as colluvium or glacial till. They often initiate within rock slide deposits or colluvium and/or till-mantled hillslopes that are too steep to form a thick soil profile. Compressional ridges and internal levees were frequently observed in the deposits, indicating energetic transport and internal deformation. Open-slope debris flows are mapped like earth flows with polylines tracing internal scarps and separate polygons encompassing the upper bounding scarp and deposit.

2.3.2.3 Falls

Rockfall (RF; Figure 2.3) was the only type of fall that was observed in GTNP. These coarse deposits are found on gentle to moderately steep talus slopes beneath bare cliff faces, especially where vertically jointed sedimentary, intrusive, and metamorphic lithologies intersect glacially-oversteepened high relief topography such as Garnet Canyon and the Death Canyon Shelf. Following Cruden and Varnes (1996), we are grouping rock avalanches with rockfall. These produce similar deposits, but with a more extensive runout zone. Because rockfall was observed to some degree on nearly all steep slopes, mapped deposits are limited to constructive features that we interpreted to be primarily a product of thousands of years of episodic rockfall events. For example, sporadic rockfall that occurs on moraines and colluvial slopes was not mapped if the boundaries of a unique deposit could not be distinguished from the underlying feature. Source area polygons encompassing all continuous steep terrain that may have contributed material to each deposit are also mapped.

2.3.2.4 Topples

Rock topple (RT) was the only type of topple that was observed in GTNP. Like rockfall, rock topple produces coarse deposits on gentle to moderately steep talus slopes beneath steep cliff faces that are often a product of glacial sculpting and debuttressing. This process was primarily observed on vertically-jointed sedimentary dip slopes and intrusive igneous and metamorphic units with exfoliation joints that often have tension cracks that parallel the escarpment and are spaced at 1-5 m intervals. These tension cracks were traced with polylines and encompassed within source area polygons.

2.3.2.5 Complexes

Complexes (C; Figure 2.3) encompass all deposits that are the product of multiple styles of movement. They are classified sequentially from the *primary event* in which movement initiated to subsequent failures in the order they were interpreted to occur. For example, we frequently observed rotational rockslides that were remobilized as earth flows as the soil overlying the mobilized rock disaggregated due to oversaturation (Cruden and Varnes, 1996). These deposits are categorized as “RS-R/EFL”. A second common complex consists of rock topple and rockfall since these two processes initiate in the same settings. Complexes are mapped following the symbology of their primary movement. Distinct movements within a larger complex were mapped separately only if they were remobilizations with distinct head scarps that occurred independent of the initial movement and are visible at the 1:4,000 scale.

2.3.2.6 Rock Glaciers

Rock glaciers are masses of boulders, ice, and earth that slowly flow downward under the force of gravity. They can be comprised of an ice mass mantled by rock or rock with interstitial ice (Knight, 2019). Although the Cruden and Varnes (1996) taxonomy does not classify rock glaciers as mass movements, they are distinctive mobile features that facilitate downslope mass transport in the Teton landscape and the deposits are potentially confused with landslide deposits. Thus, we chose to map them as separate feature classes and omit them from the statistical analysis. Rock glaciers are commonly observed in north-facing cirques typically characterized by high elevations and perennial snowfields. The cirques are often ringed by cliffs that supply coarse material to the head of the deposit via topple, rockfall or other mass wasting processes. Rockfall deposits were mapped separately if their less-mobile talus cones could be easily distinguished from the adjacent rock glacier. Although rock glaciers share the “ropy” texture often observed in terminal moraines and protalus ramparts, they were distinguished from these stationary landforms by an upper domain bounded by levees paralleling the flow direction that indicate an accelerating transport rate, a lower domain in which multiple nested compressional ridges that are oriented transverse to the flow direction indicate a slowing transport rate, and a lobate, steep-faced toe. Although the entire deposit maintains a coarse, bouldery texture, the upper reaches are often unvegetated and covered by perennial snowfields while the toe can be vegetated. Each rock glacier is mapped with a polygon enclosing the entire mobile mass but not the source area.

2.3.2.7 Suspected Movements

Features that appear to be a product of mass wasting but cannot be classified in any of the aforementioned categories are mapped as <u>suspected movements</u>. These include the products of creep processes, such as solifluction and gelifliction lobes, and fans that have steep catchment areas capable of generating channelized debris flows but lack the diagnostic leveed channels and coarse texture. Each suspected movement is mapped with a polygon enclosing the entire deposit but not the source area. Because they are not definitively classified as landslides, suspected movements were omitted from the statistical analysis.

2.3.3 Descriptive Statistics

Descriptive statistics measuring the central tendency, variability, and distribution of the attributes derived for the inventory dataset reveal numerous insights into the topographic and geologic domains in which mass movements initiate. Since positively-skewed distributions were observed for slope, vertical relief, and surface roughness, we chose to report median and interquartile range rather than the more commonly-reported mean and standard deviation (e.g., Butler, 2013; Crawford, 2020; Pánek et al., 2019). These statistics are tabulated in Table 2.1 for the four movement styles, bulk inventory, and study area.

The distributions of the six topographic variables were also visualized with violin plots, box plots, and rose diagrams. Figure 2.5 compares the characteristics of the bulk inventory to the study area and Figure 2.7 compares the four movement styles. Several outliers were eliminated from the surface roughness and plan and profile curvature plots to better visualize the values in which most values differ. Finally, bar plots illustrate how each of the four substrate lithologies are distributed between each movement style, the bulk inventory, and the bulk study area (Figure 2.6). Appendix 6 compares these percentages in a tabular format.

2.3.4 Geostatistical Analysis

The nearest neighbor test calculated a ratio of about 0.42 and p-value of <0.000005 (Appendix 2). This indicates that there is a strong, statistically significant clustering pattern in the distribution of mass movements throughout GTNP. In addition, Syrjala's test produced small p-values ($p<0.01$) for all six pairwise comparisons made between the kernel density distributions of each movement style (Appendix 3). This strongly supports the alternative hypothesis that the four movement styles occur in unique settings.

The two-sample K-S Test produced small p-values ($p<0.01$) when the cumulative distributions of slope, vertical relief, aspect, surface roughness, and plan and profile curvature in the bulk landslide inventory were each compared to their respective cumulative distributions throughout the bulk study area (Appendix 4). This supports the alternative hypothesis that for each of these six topographic variables, the values sampled from landslide-producing topography originated from a distinct cumulative distribution than that of the bulk study area.

The Kruskal-Wallis test produced small p-values ($p<0.01$) when the distributions of slope, vertical relief, surface roughness, and plan and profile curvature were each compared between the four movement styles (Appendix 5). This supports the alternative hypothesis that for each of these five topographic variables, the values sampled from one or more movement styles originated from a distinct population. Conversely, the Kruskal-Wallis test produced a larger p-value ($p=0.156$) when the values of aspect were compared. This is consistent with the null hypothesis that movement direction does not influence the style of failure. As such, we did not perform a post-hoc test on the aspect data.

Among the five significant topographic variables on which Dunn's multiple comparison test was performed, slope was the only variable for which all six pairwise comparisons produced small p-values ($p<0.01$; Appendix 5). This supports the alternative hypothesis that the slopes of all four movement styles were sampled from four distinct populations. Dunn's test also produced small p-values ($p<0.01$) for several additional pairwise comparisons among the four remaining variables (Appendix 5). It appears that vertical relief can distinguish earth flows and slides from rockfall/topple and debris flows, but larger p-values cast doubt on its ability to distinguish earth flows from slides ($p=0.0181$) and rockfall/topple from debris flows ($p=0.242$). Topographic surface roughness appears to distinguish debris flows from rockfall/topple but cannot distinguish earth flows and slides ($p=0.665$). Plan curvature appears to distinguish debris flows from the other movement styles but cannot distinguish earth flows, slides, or rockfall/topple. Finally, profile curvature appears to distinguish debris flows and rockfall/topple, but cannot distinguish earth flows from slides ($p=1$).

The R^2 values calculated for the Kruskal-Wallis tests indicate that the strength of variation between groups greatly varies between the topographic variables. Slope and vertical relief have the highest coefficients, at about 0.66 and 0.49 respectively, while aspect and profile curvature have the lowest values of about 0.005 and 0.08 respectively. Plan curvature and topographic roughness both have a moderate R^2 value of about 0.37.

Lastly, the chi-square test produced a very small p-value (p=1.48E-224) when the overall distribution of movement lithologies was compared to that of the bulk study area (Appendix 6). This supports the alternative hypothesis that mass movements originate from a distinct distribution of lithologies than those observed throughout the bulk study area. The chi-square test likewise produced small p-values ($p<0.01$) when the lithology distributions observed for each mass movement style was compared to that of all mass movements (Appendix 6). This is consistent with the alternative hypothesis that the four mass movement styles initiate in unique lithological settings.

2.4 Discussion

2.4.1 Do Mass Movements Occur in Unique Domains?

As previously mentioned, our first statistical objective investigates the extent to which landslide-producing topography is different from that of the encompassing region. Descriptive statistics informed by statistical analysis (Table 2.1; Figure 2.5) reveal that mass movements are not randomly distributed throughout the park, but rather cluster in unique settings. Compared to the bulk study area, here defined by the LiDAR extent minus the lakes, river floodplains, and outwash terraces in which no movements were observed, mass movements preferentially initiate on slopes that are steeper, rougher, higher-relief, more upwardly concave, and more north-south oriented than those observed throughout the bulk study area. This explains why most movements are clustered in the steep, high relief slopes west of the Teton Fault that are a product of the range's glacial legacy and rapid surface uplift (Figures 2.3, 2.4). These results are consistent with those presented in a similar study in the by Pánek et al. (2019), which found that movements in the Czech Republic's Carpathian Mountains most frequently occur on steep, high-relief, and north-south oriented slopes.

Although these findings describe broad trends in the dataset, they do not consider biases that arise from differing abundances of movement styles. For example, debris flows and rockfall/topple preferentially initiate on hillslopes with a greater surface roughness and vertical relief than the bulk study area, whereas earth flows and slides preferentially initiate on smoother, lower-relief hillslopes than the study area (Table 2.1). However, since the inventory contains more than twice the number of debris flow and rockfall/topple deposits than earth flows and slides (Figure 2.4), the bulk inventory's descriptive statistics do not reflect the terrain in which earth flows and slides initiate. Likewise, although Figure 2.5 suggests that mass movements in GTNP preferentially initiate on north and south-facing slopes, this is only true for the debris flows and rockfall/topple that dominate the range's east-west oriented glacially-oversteepened canyons (Figure 2.4). Earth flows and slides are rather more likely to initiate on eastern aspects (Figure 2.7).

Mass movements were also found to preferentially initiate in certain lithologies (Figure 2.6). For example, over half of the movements initiate in intrusive and metamorphic rocks even though these lithologies cover about 22% of the bulk study area. Conversely, only 6.3% of movements initiate in surficial deposits even though these deposits cover about 55% of the bulk study area (Appendix 6). However, these findings should be interpreted with discretion since many deep-seated movements that initiated in locations mapped as surficial deposits were assigned a bedrock substrate lithology interpolated from adjacent hillslopes.

2.4.2 Are Movement Styles Clustered in Unique Domains?

Our second statistical objective addresses whether different mass movement styles are clustered in unique domains. Descriptive statistics informed by statistical analysis reveal that the four mass movement styles do occur in distinct locations throughout GTNP. Slope and substrate lithology appear to be the strongest controls on movement style because additional statistical tests produced small p-values ($p<0.01$), suggesting that these variables can differentiate all four movement styles. Moreover, a relatively high R^2 value of 0.66 indicates that two thirds of the overall variance in slope can be explained by movement style. Overall, earth flows and slides preferentially initiate on moderate slopes of about 20° and 26°, respectively, while debris flows and rockfall/topple respectively initiate on steep to very steep slopes of about 39° and 67° (Table 2.1). Movements also preferentially initiate in differing lithologies. Debris flows and rockfall/topple overwhelmingly occur in intrusive and metamorphic lithologies whereas slides and earth flows primarily occur in sedimentary and extrusive igneous rocks (Figure 2.6).

Small p-values ($p<0.01$) produced by statistical tests also suggest that vertical relief, surface roughness, and plan and profile curvature can distinguish certain movement types. For example, profile curvature, vertical relief, and surface roughness can distinguish rockfall/topple and debris flows from earth flows and slides. Additionally, surface roughness and plan and profile curvature can distinguish debris flows from rockfall/topple. Vertical relief also appears to distinguish earth flows from slides. However, comparatively low R^2 values reveal that that only 8-49% of the overall variance in these four variables can be explained by movement style. This suggests that that even though these variables can distinguish certain types of failures, they are less powerful predictors than slope.

Although a larger p-value (p=0.156) suggests that aspect cannot distinguish any of the movement styles at a statistically significant level, descriptive statistics illustrate that on average, debris flows preferentially initiate on south facing slopes whereas rockfall/topple preferentially initiates on north and northeast-facing slopes (Table 2.1; Figure 2.7). We hypothesize that this correlation is largely controlled by the contrasting amount of solar insulation received by north and south facing slopes. On shaded north-facing slopes, freezing temperatures and snow persist for a greater duration of the year than on south-facing slopes, which are subject to more solar insulation, and consequently, more freeze-thaw cycles. This causes more snowmelt and disproportionately creates a longer time period in which liquid melt water is present south-facing slopes. Since liquid water facilitates debris flow transport, this process dominates on south-facing slopes. With that said, the extremely low R^2 value reveals that only 0.5% of the overall variance in aspect can be explained by movement style. As such, aspect is not a reliable predictor of movement style.

By identifying the topographic and geologic domains controlling where movements are most likely to occur, we can explain why certain movement styles are clustered in different areas of GTNP. For example, the places where rockfall/topple and debris flows are most densely clustered (Figure 2.4) co-occur with the steep, high-relief slopes underlain by intrusive/metamorphic lithologies that are concentrated on the flanks of the high peaks west of the Teton Fault where the greatest glacial exhumation has occurred (Figures 2.1, 2.3; Foster et al., 2010). Likewise, the areas where earth flows and slides are most densely clustered (Figure 2.4) co-occur with the moderate, lower-relief slopes underlain by sedimentary/extrusive lithologies and surficial deposits that are concentrated on the lower peaks bounding the Teton Range to the north and south and the rolling hills east of the Teton Fault (Figures 2.1, 2.3). These observations corroborate Pánek et al. (2019), who also found that movements of the same type tend to cluster in the topographic and lithologic settings.

2.4.3 Limitations

One limitation of this study is that our field-based data validation process was inherently biased. Because large sections of GTNP are inaccessible by road or trail, we had to rely on the LiDAR data, aerial imagery, and the Love et al. (1992) map to ground truth the classification and substrate lithology of movements in the remote corners of the park. This is a potential source of error in the statistical analysis because it was often difficult to determine whether prehistoric landslides dominantly mobilized earth or debris without direct field observations because colluvial cover masks the original texture. Moreover, field observations were only viable where the movement was accessible and had outcrops or stream incision exposing its interior. Therefore, we suggest that one can most accurately implement the Cruden and Varnes (1996) taxonomy to describe recent or historic movements but will face greater uncertainty classifying prehistoric movements.

This data validation bias might also reflect a mapping bias. In particular, discrete rockfall/topple deposits were often difficult to distinguish from adjacent colluvium and glacial deposits without field observations because they share a similar texture in the LiDAR slope layer. This may help explain why rockfall/topple are most frequently mapped in the easily accessible canyons of the southern Tetons but are mapped less frequently in the inaccessible yet similarly steep terrain of the northern Teton Range.

Although the inventory identified a variety of movement types, it is by no means exhaustive. For example, we observed active earth fall/topple and debris fall/topple features along river channel cut banks that were too small for the 1:4,000 mapping scale. Consequently, these smaller movement styles were omitted from the inventory. Conversely, although no spreads were observed in the study area, we believe that they have occurred in the past, given the region's active seismicity and the extensive wetlands adjacent to the Snake River and Jackson Lake.

2.4.4 Applications to Existing and Future Studies

Descriptive statistics reported by Buter (2013) on the slope, aspect, and standard curvature of channelized debris flows, rockfall, and rock slides observed in five canyons draining the southeastern part of the Teton Range allow us to perform a limited validation of our statistical findings. Although Butler's (2013) findings corroborate the median slope, aspect, and curvature values we derived for debris flows and rockfall/topple (Table 2.1), they are not consistent with the attributes we measured for slides. Butler (2013) suggests that rock slides preferentially initiate on planar to slightly convex north-facing hillslopes with a very steep average slope of about 54°, while we found that slides tend to initiate on planar east-facing hillslopes with a much lower median slope of about 26°. One explanation for this discrepancy is that most of the mapped slides are clustered in the northern and eastern parts of GTNP, where there is a greater occurrence of moderate east-facing slopes than in the five canyons that comprise Butler's study area, which are dominated by steep north- and south-facing slopes (Figures 2.3, 2.4).

A second explanation for the lack of agreement is the method by which Butler (2013) measured the rock slides' topographic attributes. Because landslides modify the topography in which they initiate, the topographic attributes measured for a given movement will vary based on where and how they are measured. Although we attempted to describe the unmodified topography that produced each slide by extracting topographic attributes from hillslopes laterally adjacent to each deposit (Figure 2.2), Butler measured these attributes from source point features positioned directly upslope of each deposit. This lack of consistency is common to all landslide susceptibility studies, which have also used source point features positioned in the deposit centroid (e.g., Crawford et al., 2021) and "seed cells" randomly generated in the unmodified topography adjacent to each movement's head scarp and flanks (e.g., Suzen and Doyuran, 2004).

The area of the zones from which these values are calculated also varies between studies. Butler (2013) derived his topographic values from point features whereas the mean values within 10-30 m radius circular buffers were calculated here (Figure 2.2). We argue that the buffer radius should match the scale of the topography that is being measured. Larger radii capture larger topographic trends whereas smaller radii and points are more sensitive to "noise," or local variation in the DEM, as evidenced by the larger standard deviations in Butler's reported values.

These methodological inconsistencies in measuring topographic attributes highlight the need for an established landslide characterization protocol. Reichenbach et al. (2018) notes that most landslide susceptibility studies use a statistical approach in which logistic regression evaluates the extent to which each variable predicts the presence and absence of mass movements in a given domain. The problem with this is that when a model is trained with "presence points" derived from the mass movement deposits and "absence points" derived from the region outside of known mass movement features, it is actually predicting the presence of landslide deposits, rather than landslide-producing topography. Consequently, landslide susceptibility maps constructed with this approach may mis-assess unmodified hillslopes that are susceptible to failure. However, the subjectivity with which we inferred what constitutes landslide-producing topography highlights the difficulty of implementing these changes within a logistic regression framework. In particular, generating "absence points" that do not intersect unmodified landslide-prone topography will require robust descriptive statistics of the topographic and geologic domains in which movements initiate.

One challenge to implementing a standardized susceptibility modeling protocol is the varying availability of high-resolution elevation datasets. Even though global LiDAR coverage is rapidly expanding, 10 m is still the highest spatial resolution available for many global locations. Although the absence of a high-resolution bare-earth DTM greatly reduces the accuracy and precision with which movements can be mapped (McKean and Roering, 2004), the similarities between the slope and curvature values Butler (2013) and this study derived for rockfall and debris flows suggests that accurately measuring topographic variables is still possible with a coarse DEM. With that said, Butler's (2013) study area was constrained by largely-unforested alpine terrain where rockfall deposits and debris flow fans are clearly visible in satellite imagery. Further research is required to discern whether this assumption holds true in forested landscapes where there might be a greater discrepancy between landslide inventories created with and without a bare-earth DTM.

2.5 Conclusions

To better understand where and how mass movements occur in steep, high-relief landscapes, we paired digital mapping with field observations to create a landslide inventory map encompassing GTNP. The topographic and geologic diversity of the Teton landscape is reflected by the wide variety of movement styles observed. Compared to the bulk study area, mass movements in GTNP occur on steep hillslopes with greater local vertical relief and topographic surface roughness and upwardly concave plan and profile curvatures (Figure 2.5).

Grouping the movements into four generalized classes and performing further geostatistical investigations reveals that mass movement styles occur in unique topographic and geologic domains. Debris flows preferentially initiate on steep (~39°), high-relief, concave, south-facing hillslopes that have a relatively high surface roughness and overlie intrusive and metamorphic lithologies. Rockfall/topple preferentially initiates on very steep (~67°), high-relief, convex, northeast-facing hillslopes that have a relatively high surface roughness and overlie intrusive and metamorphic lithologies. In contrast, earth flows preferentially initiate on gentle (~20°), lower-relief, planar, northeast-facing hillslopes that have a relatively low surface roughness and overlie sedimentary and extrusive lithologies and surficial deposits. Finally, slides preferentially initiate on moderate (~26°), moderate-relief, planar, east-facing hillslopes that have a relatively low surface roughness and overlie sedimentary and extrusive lithologies. The strong spatial clustering observed for each of these four movement styles (Figure 2.4) reflects how the topographic and lithologic domains most favorable for their development co-occur in specific areas of the park (Figures 2.1, 2.3).

By identifying these patterns in where and how past landslides preferentially occur, our inventory and statistical findings serve as the foundation for all future efforts to characterize landslide hazards in GTNP and assess the risks they pose to visitors and infrastructure. This includes developing park-wide landslide susceptibility models that predict the likelihood of future events based off the domains in which past events occurred. Since the various movement styles preferentially initiate in differing topographic and geologic domains, we emphasize that a single generalized landslide susceptibility model may be a less powerful tool than multiple susceptibility models optimized for individual movement styles. For example, a localized rockfall event not only occurs in a different location, but also presents a different risk to people and infrastructure than a slow-moving earth flow complex and likewise requires different mitigation measures.

Chapter 2 Figures

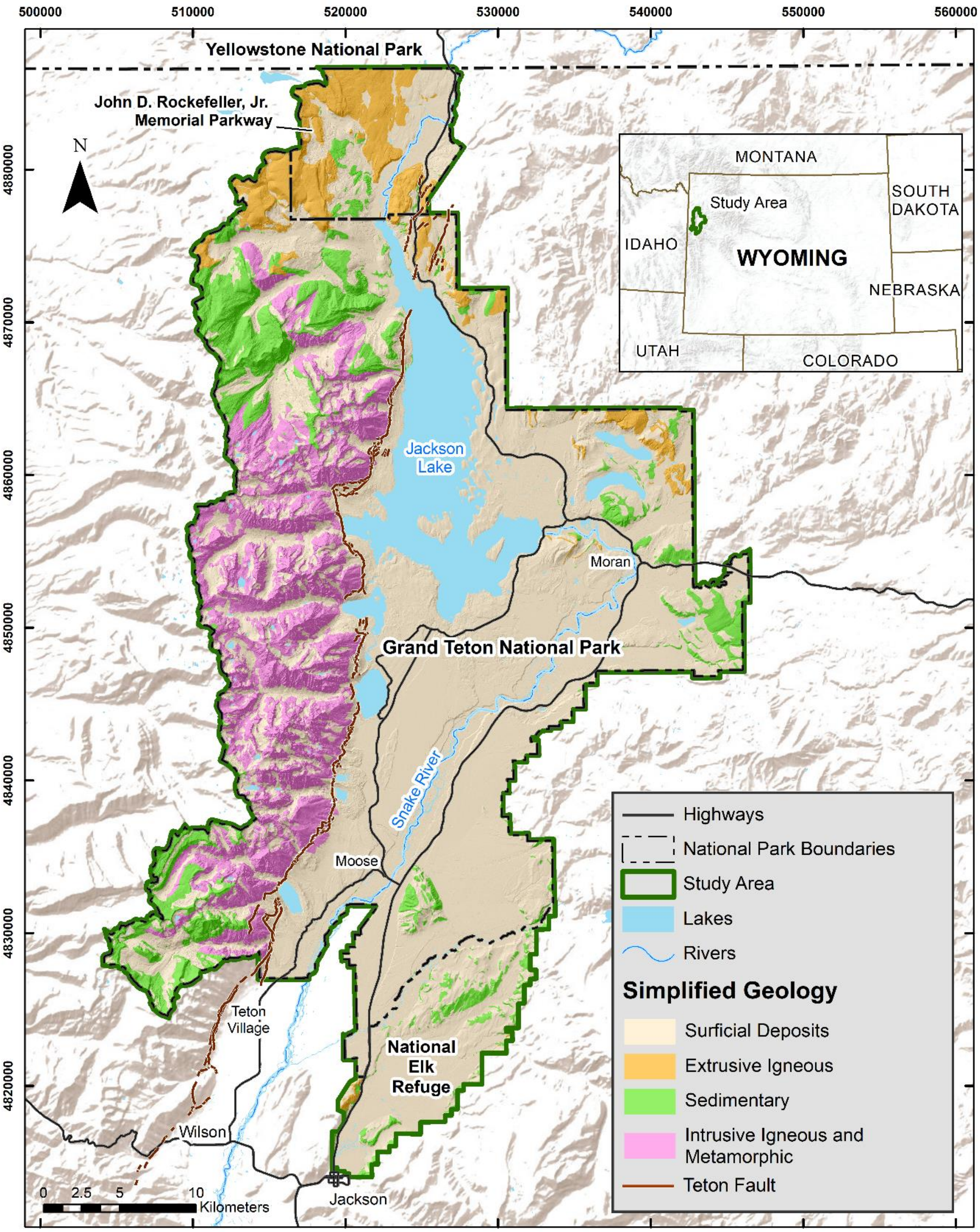

Figure 2.1: Overview map of the study area (outlined in green). The geologic units defined by Love et al. (1992) have been aggregated into four rock types based on their age, rheology, and co-occurrence in the park. The brown line traces the Teton Fault as mapped by Zellman et al. (2019). The measured grid is in NAD 1983 UTM Zone 12N. Hillshade basemap and transportation data courtesy of ESRI.

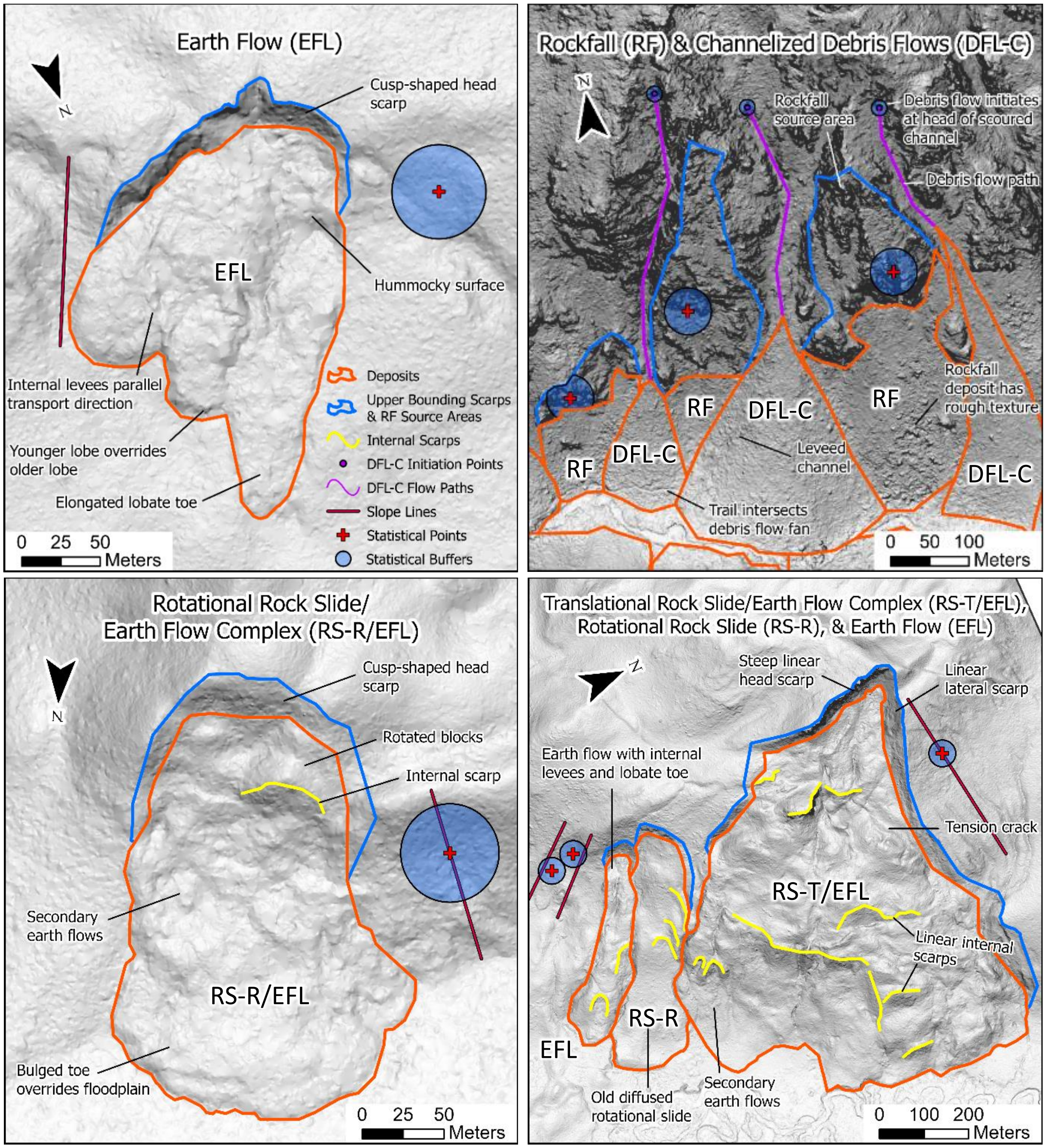

Figure 2.2: Annotated slope maps of several of the most common movement styles and examples of their diagnostic features observed (top left) south of Emma Matilda Lake, (top right) in Granite Canyon, (bottom left) near Pacific Creek, and (bottom right) adjacent to Arizona Creek. The curvature, vertical relief, and surface roughness of the topography in which each movement initiated was derived from blue circular buffers adjacent to each deposit and at each channelized debris flow initiation point. Slope was derived from the red line segments and each channelized debris flow path.

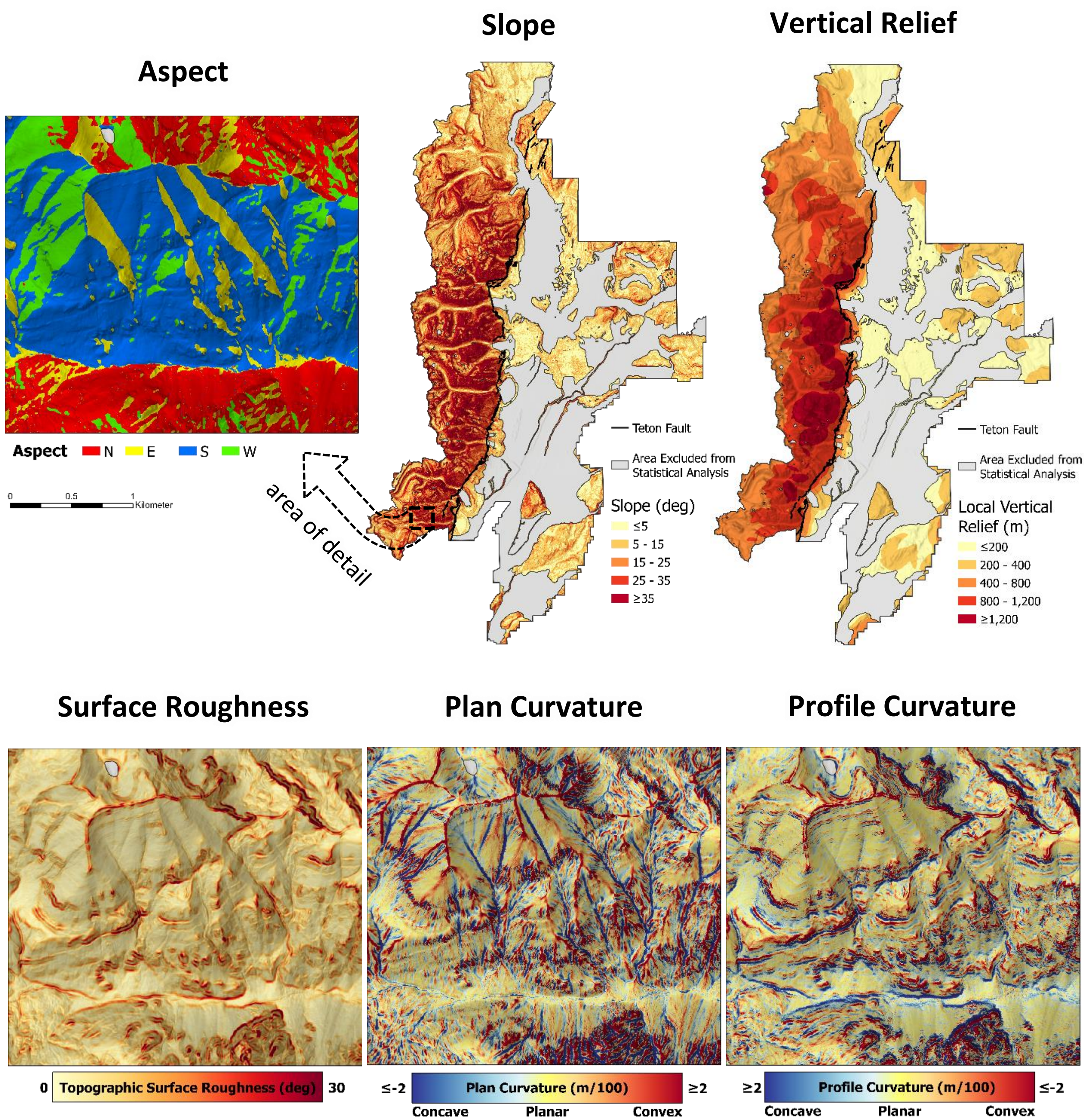

Figure 2.3: Distribution of the six topographic variables derived for each movement and the bulk study area. Slope and vertical relief are shown for the entire study area to highlight the strong contrast in their respective values east and west of the Teton Fault (shown in black). Maps of aspect, roughness, and plan and profile curvature are limited to a small area of Granite Canyon due to large local variation. Slope, relief, and aspect are classified here only for visualization purposes; their true values were used in the statistical analysis.

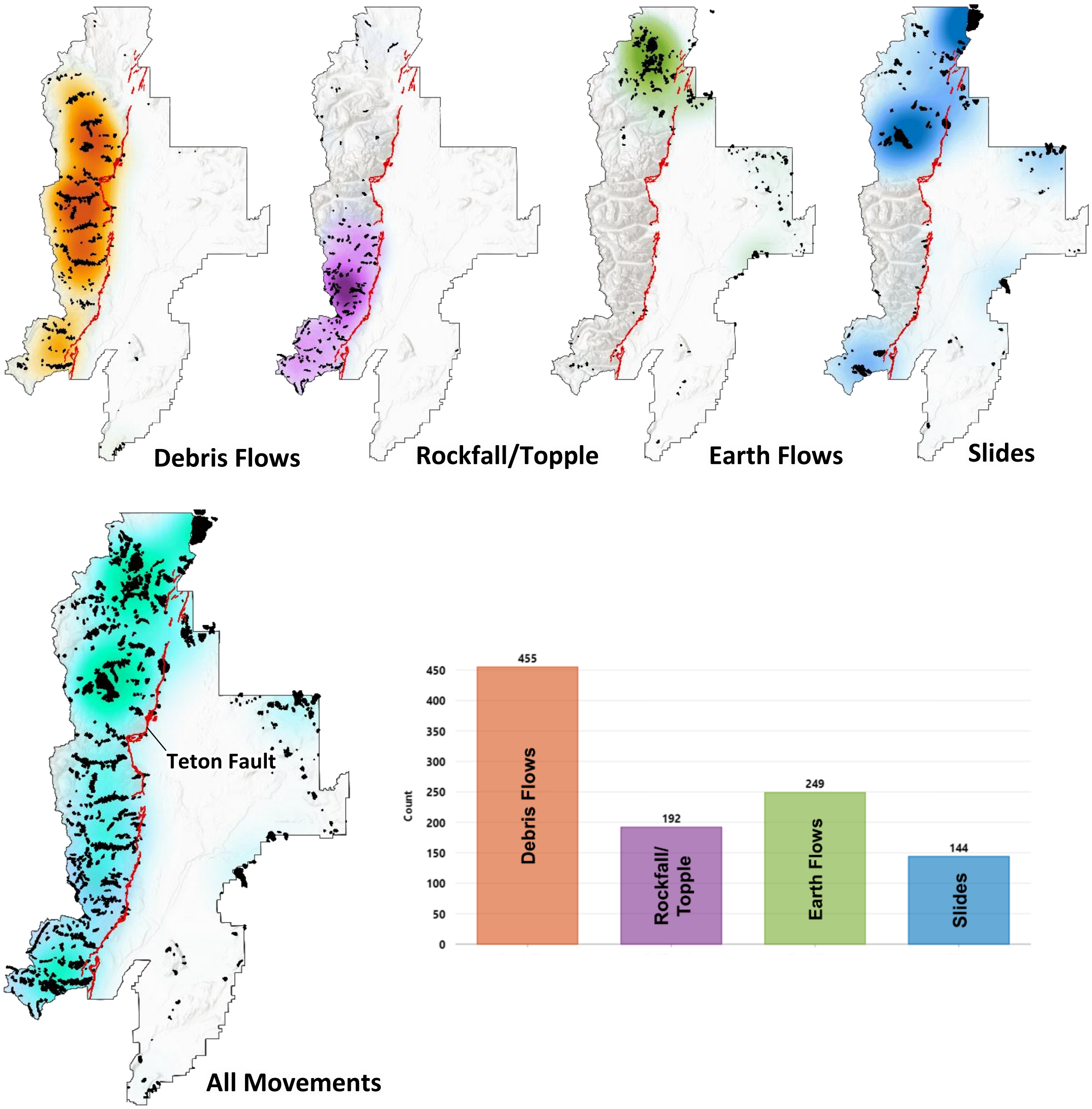

Figure 2.4: Kernel density maps of all mass movements and each of the four movement styles are overlain with the boundaries of each respective movement type (black) and the Teton Fault (red). The kernel density functions are weighted by deposit surface area to account for the size disparity between many of the movements. Darker colors indicate a higher density of deposits. The histogram compares the abundance of each movement style among the 1040 unique movements in the full inventory dataset.

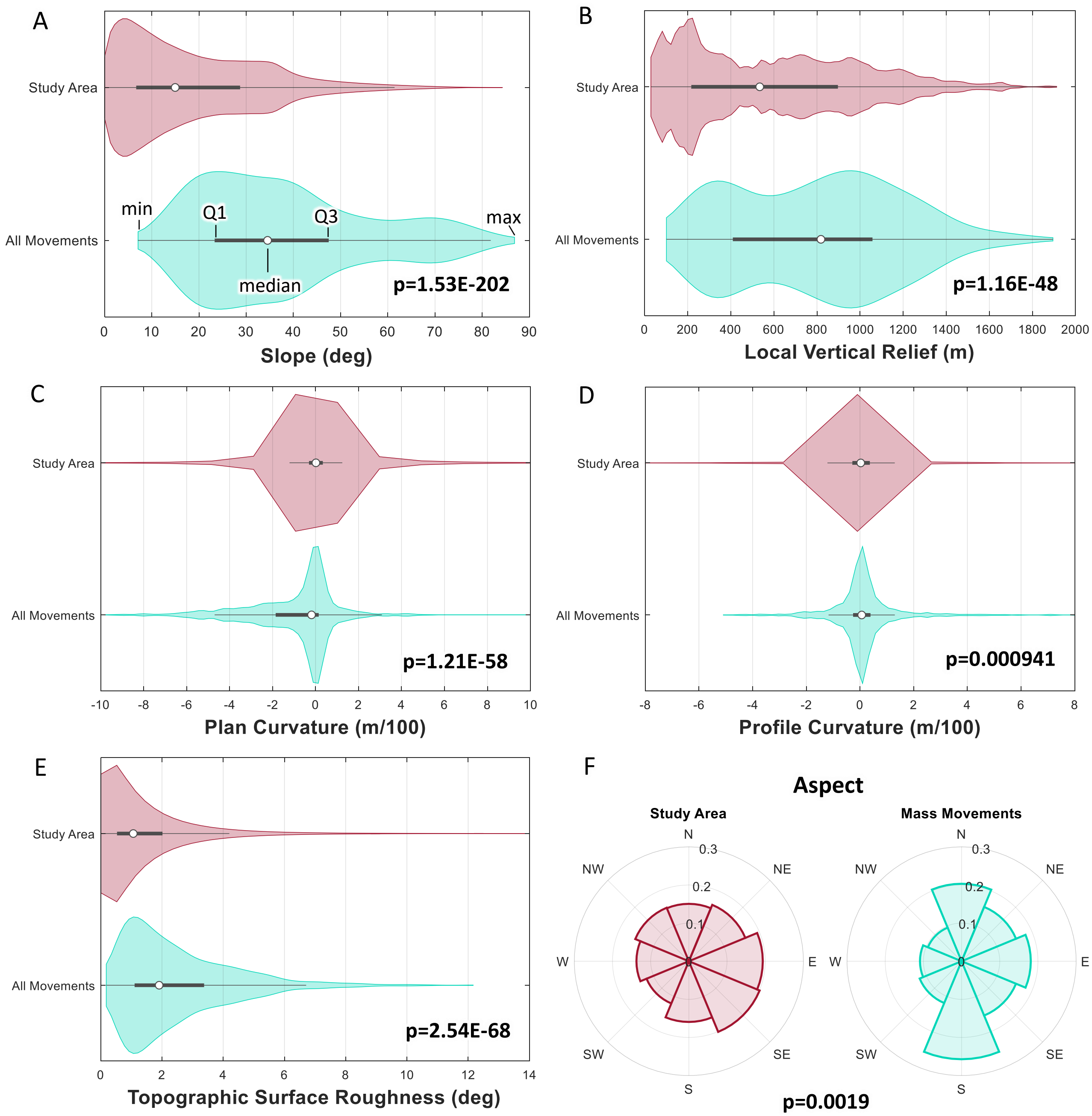

Figure 2.5: Violin plots in which kernel distribution functions normalized by probability density compare the (A) slope, (B) local vertical relief, (C) plan curvature, (D) profile curvature, and (E) topographic surface roughness of the bulk study area (red) with that of all mass movements (blue). Box plots indicate the median and upper and lower quartiles. Values beyond the length of each whisker (1.5 times the interquartile range) are considered outliers (MathWorks, 2022). Several extreme outliers are not shown in the plan and profile curvature plots to emphasize how the two distributions differ at low curvature values. Several outliers are eliminated from the plan and profile curvature plots to emphasize how the two distributions differ at low curvature values. (F) Rose diagrams compare the probability distribution of hillslope aspect throughout the bulk study area (red) with that of mass movement direction (blue).

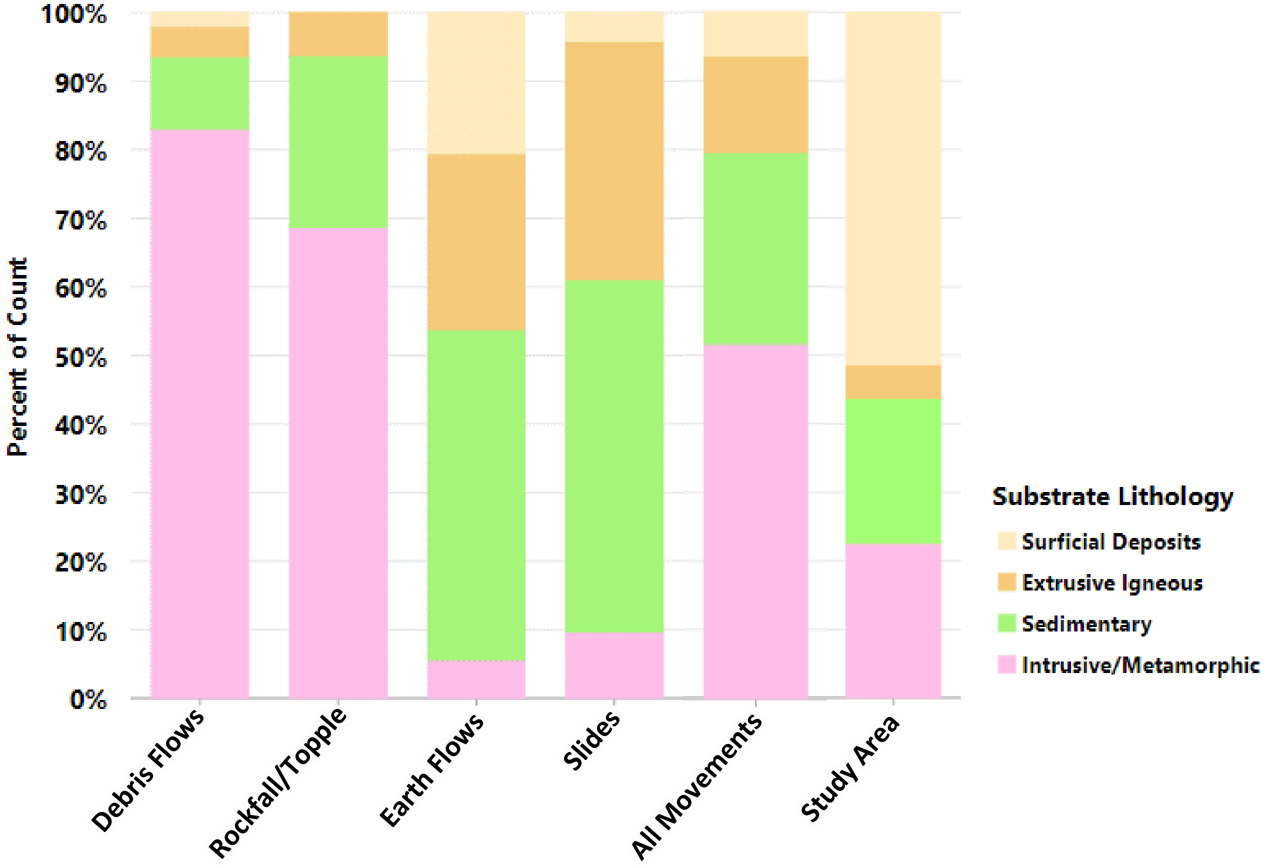

Figure 2.6: Histogram showing the relative distribution of each of the four substrate lithologies as a percentage of each movement style, the overall inventory, and the entire study area.

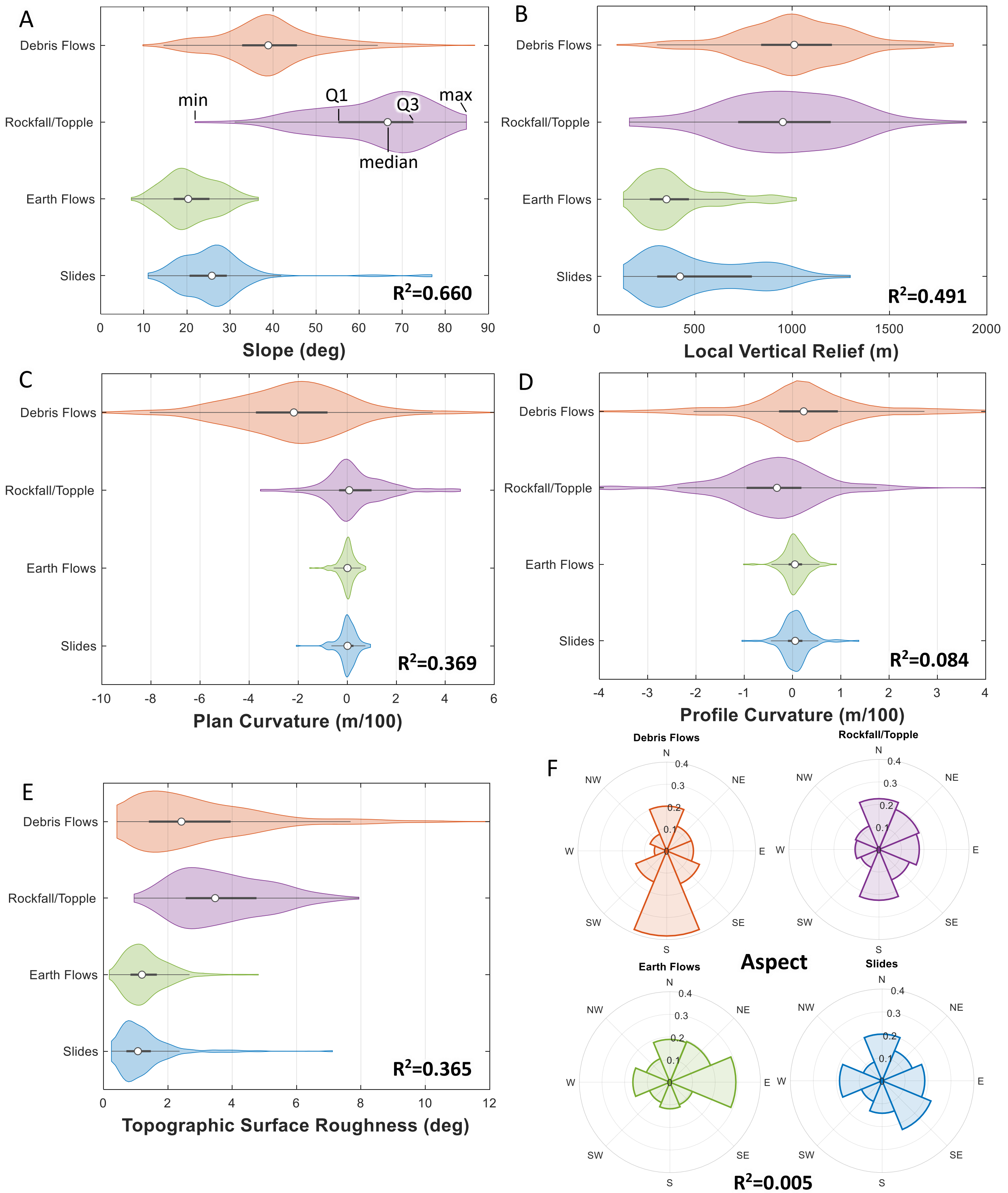

Figure 2.7: Violin plots in which kernel distribution functions normalized by probability density compare the (A) slope, (B) local vertical relief, (C) plan curvature, (D) profile curvature, and (E) topographic surface roughness of debris flows (orange), rockfall/topple (purple), earth flows (green), and slides (blue). Box plots indicate the median and upper and lower quartiles. Values beyond the length of each whisker (1.5 times the interquartile range) are considered outliers (MathWorks, 2022). Extreme outliers are not shown in the plan and profile curvature plots to emphasize how the distributions differ at low curvature values. (F) Rose diagrams compare the probability distributions of the four styles' movement directions.

Chapter 2 Tables

Table 2.1: Descriptive statistics tabulating the median topographic values and interquartile ranges (IQRs) derived for the four movement styles, the overall inventory, and the bulk study area.

	Slope (deg)		Vertical Relief (m)		Surface Roughness (deg)		Profile Curvature (m/100)		Plan Curvature (m/100)		Aspect (azimuth clockwise from north)	
	Median	IQR	Median	IQR	Median	IQR	Median	IQR	Median	IQR	Median	IQR
Debris Flows	38.89	12.53	1011.50	359.19	2.42	2.52	0.23	1.20	0.23	2.52	172.12	025.74
Rockfall/Topple	66.60	17.18	953.07	470.47	3.47	2.15	-0.32	1.12	0.08	1.29	038.79	032.85
Earth Flows	20.30	8.10	355.67	194.12	1.20	0.79	0.05	0.26	0.01	0.28	042.36	051.71
Slides	25.80	8.45	425.28	482.12	1.07	0.74	0.05	0.29	0.01	0.36	104.40	046.07
All Movements	34.53	23.96	818.32	644.27	1.91	2.25	0.06	0.62	-0.19	1.97	104.08	034.84
Field Area	14.96	21.86	534.33	677.56	1.06	1.46	0.03	0.63	0.02	0.61	097.24	045.38

Chapter 3: Conclusions

3.1 Summary

To more precisely describe where and how mass movements occur in GTNP and similar high-relief landscapes, digital mapping assisted by a LiDAR-derived bare earth DTM and detailed field observations were employed to create a 1:4,000 scale landslide inventory map documenting the position and failure style of all past mass movements in GTNP. The distribution of mapped features reveals that mass movements most frequently occur in the steep topography of the Teton Range and the lower-relief hills along the northern park boundary, yet seldom occur in the low relief glacial outwash terraces that dominate the central part of the park.

Next, the slope, vertical relief, topographic roughness, plan and profile curvature, aspect, and substrate lithology of all 1040 movements were individually measured. By calculating descriptive statistics from these topographic and geologic attributes, we were able to better characterize the domains in which different movement styles initiate. Debris flows were found to preferentially initiate on steep (~39°), high-relief, concave, south-facing hillslopes that have a relatively high surface roughness and overlie intrusive and metamorphic lithologies. Rockfall/topple was found to preferentially initiates on very steep (~67°), high-relief, convex, northeast-facing hillslopes that have a relatively high surface roughness and overlie intrusive and metamorphic lithologies. Earth flows were found to preferentially initiate on gentle (~20°), lower-relief, planar, northeast-facing hillslopes that have a relatively low surface roughness and overlie sedimentary and extrusive lithologies and surficial deposits. Finally, slides were found to preferentially initiate on moderate (~26°), moderate-relief, planar, east-facing hillslopes that have a relatively low surface roughness and overlie sedimentary and extrusive lithologies.

In addition to identifying patterns in the dataset, these seven attributes served as the basis for a twofold geostatistical analysis. We first considered whether mass movements *as a whole* occurred in unique settings. The small p-values produced by statistical tests ($p<0.01$) suggest that mass movements are not randomly distributed throughout the park, but are rather clustered into unique domains with topographic and geologic attributes that differ from those of the bulk study area. Next, we considered whether the four categories of movement styles occur in unique locations, and if so, which attributes best explain their clustering. The small p-values ($p<0.01$) produced by additional statistical tests suggest that the four movement styles have unique spatial distributions that are best explained by variations in slope and substrate lithology. Vertical relief, surface roughness, and plan and profile curvature appear to have limited discriminatory power since larger p-values ($p>0.1$) suggest they could only distinguish one to three movement styles. This is reflected by lower R^2 values and overlapping distributions. Finally, a large p-value ($p=0.156$) and small R^2 value ($R^2=0.005$) suggest that aspect cannot distinguish between any of the movement styles at a statistically significant level.

3.2 Limitations

One of the limitations inherent to landslide inventory mapping and classification is that prehistoric landslide deposits seldom constitute a singular event, but rather are the product of repeated remobilizations and diffusive processes that act to modify the initial movement over hundreds to thousands of years (Hungr et al., 2014). If these later events have obscured the diagnostic features of the initial movement, then it is possible that we misclassified the primary movement of older complexes. For example, we observed many debris flow fans in steep gullies bounded by cliffs that are capable of producing rockfall. Although it is likely that the coarse material in the fan is a product of both falls and flows, it is difficult to determine the initial movement. This is also true for rockfall/topple complexes. This nuance highlights the limitations of a statistical approach that considers only one mode of transport when it is widely acknowledged that most movements are complexes (Cruden and Varnes, 1996).

These are also limitations to classifying movements with LiDAR alone. For example, many of the large movements that were observed in the isolated northwestern region of the park and classified as earth flows may have initiated as translational or rotational rockslides. One explanation for this is that slides tend to disintegrate into multiple smaller units as velocity and/or travel distance increases (Campbell, 1985; Highland and Bobrowsky, 2008). Because these smaller units increasingly-resemble the hummocky topography diagnostic of earth flows, we may have misclassified older, soil-mantled slides as earth flows. We hypothesize that following the initial slide, the internal drainage of the displaced mass is modified to force water to the surface near the toe. The steep, oversaturated toe subsequently fails as an earth flow.

Classification errors also have ramifications for statistical analysis. If a large portion of slides were misclassified as earth flows, that could help explain why statistical tests suggest that they cannot be differentiated by plan and profile curvature, surface roughness, and aspect. An alternative explanation is that slides and earth flows do indeed co-occur in similar topographic domains and are rather more readily distinguished by soil thickness and other geologic parameters not examined here.

Finally, a lack of historical observations and geochronological data limits our ability to definitively characterize the age and temporal frequency of mass movements in GTNP. However, our understanding of the local paleoclimate and predisposing and triggering factors allows us to speculate on this issue (Figure 3.1). Based on the present distribution of mass movements and the maximum extent of the Pinedale glaciation (Pierce et al., 2018), we propose that the movements presented in this inventory have dominantly occurred in the ~15 kyr following the LGM. Thus, we expect the ratio of new movements to reactivations of existing movements to decrease over time.

We also propose that the frequency of mass movements has fluctuated over time, with spikes in frequency potentially tied to glacial, climatic, and seismic forcings. For example, we expect to see a higher frequency of movements immediately following the LGM due to retreating glaciers debuttressing oversteepened hillslopes and a lack of stabilizing vegetation. This is supported by the rapid deposition of non-glacial sediments with low concentrations of organic matter into Jenny Lake at the start of the early Holocene (Larsen et al., 2016). While the effects of debuttressing have diminished over time as the freshly-deglaciated hillslopes are colonized by vegetation and adjusted by mass wasting to more stable geometries, (Larsen et al., 2016), other forcing may become more dominant. For example, mass movement frequency may fluctuate in response to climate variation, since more intense precipitation increases pore water pressure (Crozier, 2010; Highland, 2008) and a warmer and/or drier climate is more favorable to more frequent or intense wildfires that denude the landscape of stabilizing vegetation (Highland, 2008; Flannigan et al., 2006). Finally, seismic events have been tied to historic (e.g., Blackwelder, 1912; Hadley, 1964) and prehistoric (e.g., Tranel and Strow, 2017) movements in the region.

3.3 Future Work

3.3.1 Significance

This landslide inventory provides a means for park officials to identify where existing mass movements intersect roads, trails, and other vulnerable infrastructure. Because existing movements are prone to reactivation, this inventory provides a first-order assessment of where future failures may occur. In addition, the statistical analysis offers a second-order assessment of the topographic and geologic domains in which specific movement styles tend to initiate (Figure 3.2). The strong clustering pattern observed between the four movement styles reflects how their controlling topographic and lithologic domains likewise co-occur in specific areas of the park. These statistical findings also serve as the basis for future third- and fourth-order assessments of susceptibility and risk (Figure 3.2). Since different failure styles present different risks and require different mitigation measures, it is important to understand how future mass movements are likely to occur. For example, rockfall and debris flow damage was frequently observed throughout the western part of the park where trails followed the bottom of glacially-sculpted valleys or traversed boulder fields beneath steep cliffs. Conversely, buckling roads and tipping utility poles were observed in the northeastern corner of the park where they intersected slide/earth flow complexes.

3.3.2 Improvements Needed to Support Susceptibility Mapping

Although the seven topographic and geologic attributes explored in this study are a good starting point for future efforts to map landslide susceptibility, additional work is needed to quantitatively assess the degree to which each factor is controlling where and how future mass movements will occur in GTNP. The R^2 values provide a useful measure of how well each topographic variable can differentiate movement style, but equivalent metrics cannot be calculated for substrate lithology, or any other categorical variables compared with the chi-square test.

In addition, we acknowledge that the seven variables presented here are by no means an exhaustive list of predisposing factors. One factor not addressed in this study is the influence of geologic structure. Butler (2013) determined that proximity to the Teton Fault is a statistically significant variable controlling the frequency of mass movements in five major canyons along the eastern flank of the range. He hypothesized that the active seismicity has weakened the valley walls by fracturing bedrock and exacerbating preexisting joints. Future work may evaluate the extent to which this relationship applies to the entire study area, or if it is unique to the glacially-debuttressed canyons that intersect the fault. In that case, glacial oversteepening may be the primary control on movement distribution.

A second potential geologic control on movement distribution is bedding orientation with respect to hillslope aspect. During field reconnaissance, translational rockslides and rock topple were most frequently observed on dip slopes whereas rotational rockslides were observed on anti-dip slopes. Although these observations are limited to sedimentary and extrusive lithologies, we hypothesize that joints and/or foliation may be exercising a similar control on the frequency and style of movements that initiate in intrusive and metamorphic lithologies. Although we chose not to differentiate rotational and translational slides for the statistical analysis, we hypothesize that the presence of dip and anti-dip slopes will be an important predictor in future susceptibility modeling efforts. However, since numerous faults and folds have produced large local variations in bedrock orientation, accurately interpolating this parameter at a parkwide scale will require bedrock attitude measurements to be collected at a greater density than is presently available from Love et al. (1992).

3.3.3 Best Practices for Future Researchers

Several authors, including Cruden and Varnes (1996), Burns and Madin (2009), and Slaughter et al, (2017) have suggested approaches for mapping and classifying mass movements. In this study, we recognized several ways to build upon and/or improve these authors' ideas.

Here we propose several additional "best practices" that future workers may implement in the production, characterization, and analysis of landslide inventory maps.

Landslide Mapping and Classification

- There is a need for a *single established* landslide mapping protocol that adopts a standard classification taxonomy (e.g., Cruden and Varnes, 1996) and geodatabase structure (e.g. Burns and Madin, 2009). Adhering to such a standard will facilitate easier comparisons between studies and the integration of local inventories into regional or global datasets.
- Open-slope debris flows should be distinguished from channelized debris flows because not all flows that mobilize coarse materials are confined to stream channels.
- Although rock glaciers are typically not included in landslide inventories, we recommend that they be incorporated into the inventory geodatabase as a separate feature class so they are not misclassified as mass movements in future map updates. This is also true for suspected movements.

Characterizing Inventories with Descriptive Statistics

- When characterizing an inventory, the attributes of *pre-failure topography* should be measured, rather than those of deposits or scarps. This can be interpreted from unfailed hillslopes adjacent to each movement.
- Similar movement styles should be grouped prior to statistical analysis to address small sample sizes (e.g., translational and rotational slides) and redundancy between styles that co-occur (e.g., rockfall and topple). We acknowledge that this approach is subjective, and different ways of grouping may influence statistical outcomes.
- Median and interquartile range are preferable measures of central tendency and variability to mean and standard deviation when a variable exhibits a skewed distribution.

- Circular smoothing windows are appropriate for eliminating random variation and capturing larger topographic trends when generating raster layers (slope, aspect, curvature, etc.) from a LiDAR-derived DTM. ESRI's new Surface Parameters tool may be worth integrating into future studies because it automatically adjusts the size of the moving observation window to the variability of the local terrain (ESRI, 2022c).
- Plan and profile curvature should be considered separately because they control different aspects of landslide kinematics.

Susceptibility Analysis

- A single susceptibility model is not appropriate for predicting the likelihood of all mass movement styles since different types preferentially occur in different settings. However, we acknowledge that some types co-occur in similar settings. For example, our statistical findings suggest that future GTNP susceptibility models should group earth flows and slides together unless one identifies additional attributes that differentiate these two movement styles at a statistically significant level.

Dissemination of Landslide Inventory to the Public

- ArcGIS Story Maps provide a free and easily accessible web portal for the public and stakeholders to interact with the landslide inventory geodatabase and LiDAR-derived basemaps without the need for GIS software and a computer with high processing power. Our GTNP landslide inventory has been published online in a Story Map available at this link: https://arcg.is/1aaKHi

Chapter 3 Figures

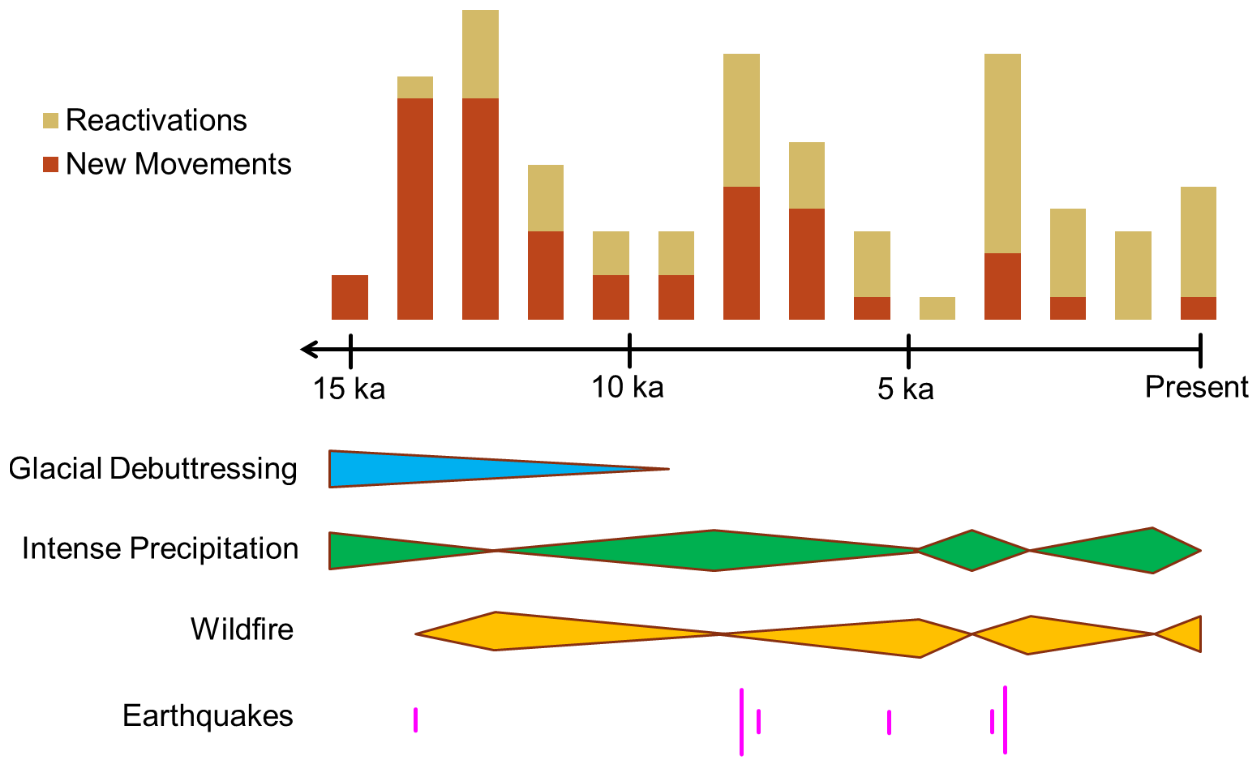

Figure 3.1: Conceptual timeline showing how the role of various predisposing factors (e.g., glacial debuttressing and wildfire) and triggering factors (e.g., intense precipitation and earthquakes) has varied over the past ~15 kyr following the LGM. Likewise, the frequency of mass movements (here represented as counts in a histogram with bin widths corresponding to equal time intervals) has fluctuated over time, with spikes in frequency potentially tied to these glacial, climatic, and seismic forcings. We also propose that the ratio of new movements (red) to reactivations (tan) has decreased over time.

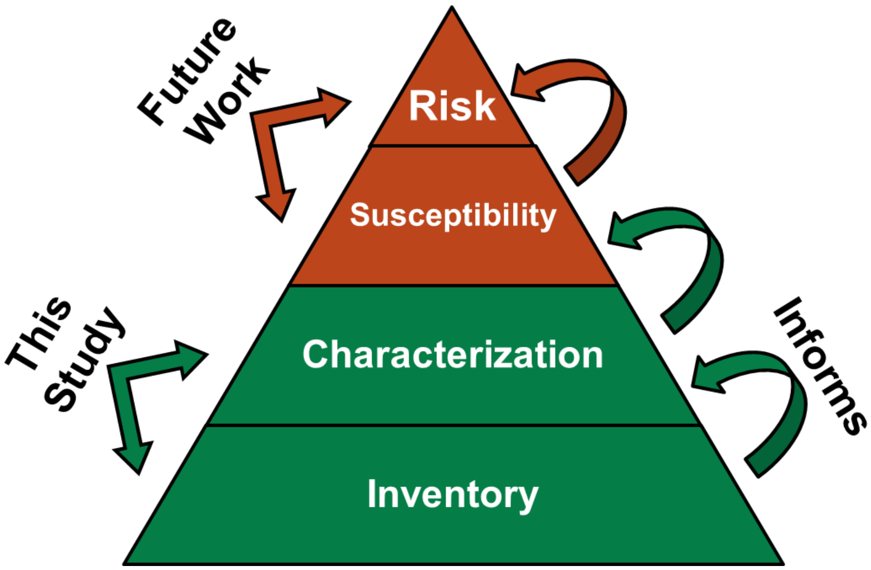

Figure 3.2: Conceptual diagram showing how the landslide inventory map and statistical analysis presented here serve the foundation of higher-order products including susceptibility models and risk assessments that may build upon these findings in future studies.

References

Bălteanu D, Micu M, Jurchescu M, Malet JP, Sima M, Kucsicsa G, Dumitrică C, Petrea D, Mărgărint MC, Bilaşco Ş, Dobrescu CF, 2020, National-scale landslide susceptibility map of Romania in a European methodological framework: Geomorphology, vol. 371, no. 107432, doi:10.1016/j.geomorph.2020.107432.

Beck, H.E., Zimmermann, N.E., McVicar, T.R., Vergopolan, N., Berg, A., and Wood, E.F., 2018, Present and future Köppen-Geiger climate classification maps at 1-km resolution: Scientific Data, vol. 5, no. 180214, doi:10.1038/sdata.2018.214.

Bellugi, D.G., Milledge, D.G., Cuffy, K.M., Dietrich, W.E., and Larsen, L.G., 2021, Controls on the size distributions of shallow landslides: PNAS, vol. 118, no. 9, 11 p., doi:10.1073/pnas.2021855118.

Bishop, M.P., 2013, Remote sensing and GIScience in geomorphology: introduction and overview, *in* Shroder, J, and Bishop, M.P., eds., Treatise on Geomorphology: Academic Press, San Diego, CA, vol. 3, p. 1–24, doi:10.1016/B978-0-12-374739-6.00040-3.

Blackwelder, E., 1912, The Gros Ventre slide, an active earth-flow: Bulletin of the Geological Society of America, v. 23 no. 1, p. 487-492, doi:10.1130/GSAB-23-487.

Boualla, O., Mehdi, K., Fadili, A., Makan, A., and Zourarah, B., 2019, GIS-based landslide susceptibility mapping in the Safi region, West Morocco: Bulletin of Engineering Geology and the Environment, vol. 78, p. 2009–2026, doi:10.1007/s10064-017-1217-y.

Brardinoni, F., Slaymaker, O., and Hassan, M.A., 2003, Landslide inventory in a rugged forested watershed: a comparison between air-photo and field survey data: Geomorphology, vol. 54, p. 179-196, doi:10.1016/S0169-555X(02)00355-0.

Brown, S. J., Thigpen, J. R., Spotila, J. A., Krugh, W. C., Tranel, L. M., and Orme, D. A., 2017, Onset timing and slip history of the Teton fault, Wyoming: A multidisciplinary reevaluation. Tectonics, vol. 36, p. 2669–2692, doi:10.1002/2016TC004462.

Bunn, M.D., Leshchinsky, B.A., Olsen, M.J., and Booth, A., 2019, A Simplified, Object-Based Framework for Efficient Landslide Inventorying Using LIDAR Digital Elevation Model Derivatives: Remote Sensing, v. 11, no. 3, 303, https://doi.org/10.3390/rs11030303.

Burns, W.J., and Madin, I.P., 2009, Protocol for inventory mapping of landslide deposits from light detection and ranging (LiDAR) imagery, Special Paper 42: DOGAMI, Portland, OR, 36 p.

Butler, W.D., 2013, Spatial patterns and impacts of slope failures in five canyons of the Teton mountains, Grand Teton National Park, Wyoming [MA thesis]: Manhattan, Kansas State University, 193 p.

Byrd, J.O.D., Smith, R.B., and Geissman, J.W., 1994, The Teton Fault, Wyoming: Topographic signature, neotectonic, and mechanisms of deformation: Journal of Geophysical research, v. 99, no. B10, p. 20095-20122.

Campbell, R.H., ed, 1985, Feasibility of a nationwide program for the identification and delineation of hazards from mud flows and other landslides: U.S. Geological Survey Open File Report 85-276, 58 p, doi:10.3133/ofr85276B.

Carrara, A., Sorriso-Valvo, M., and Reali, C., 1982, Analysis of landslide form and incidence by statistical techniques, Southern Italy: Catena, vol. 9, no. 1-2, p. 35-62, doi:10.1016/S0341-8162(82)80004-0.

Case, J.C., 1990, Preliminary landslide map of Wyoming: Wyoming State Geological Survey: Laramie, WY, 1:24,000.

Cendrero, A., Remondo, J., Bonachea, J., Rivas, V., and Soto, J., 2006, Sensitivity of landscape evolution and geomorphic processes to direct and indirect human influence: Geografia Fisica e Dinamica Quaternaria, v. 29, p. 125-137.

Chung, C.J.F., Fabbri, A.G. and van Westen, C.J., 1995, Multivariate regression analysis for landslide hazard zonation, in Geographical information systems *in* Carrara, A., and Guzzetti, F., eds., Geographical Information Systems in Assessing Natural Hazards: Dordrecht, Springer, p. 107-133.

Clark, P.J., and Evans, F.C., 1954, Distance to nearest neighbor as a measure of spatial relationships in populations: Ecology, vol. 35, no. 4, p. 445-453, doi:10.2307/1931034.

Coe, J.A., McKenna, J.P., Godt, J.W., and Baum, R.L., 2009, Basal-topographic control of stationary ponds on a continuously moving landslide: Earth Surface Processes and Landforms, vol. 34, no. 2, p. 264-279, doi:10.1002/esp.1721.

Crawford, M.M., Dortch, J.M., Koch, H.J., Killen, A.A., Zhu, J., Bryson, L.S., and Haneberd, W.C., 2021, Using landslide-inventory mapping for a combined bagged-trees and logistic-regression approach to determining landslide susceptibility in eastern Kentucky, USA: Quarterly Journal of Engineering Geology and Hydrogeology, vol. 54, no. 4, 14 p., doi:10.1144/qjegh2020-177.

Crozier, M.J., 2010, Decipherirng the effect of climate change on landslide activity: A review: Geomorphology, v. 124, no. 3–4, p. 260-267, doi:10.1016/j.geomorph.2010.04.009.

Cruden, D.M., and Varnes, D.J., 1996, Landslide types and processes, *in* Turner, A.K., and Schuster, R.L., eds., Landslides, investigation and mitigation: Washington, D.C., Transportation Research Board, Special Report 247, p. 36–75.

Dai, F., 2018, Kruskal-Wallis Test, in Allen, M., ed., The SAGE Encyclopedia of Communication Research Methods: SAGE: Thousand Oaks, p. 832-834, doi:10.4135/9781483381411.

Dunn, O.J., 1964, Multiple Comparisons Using Rank Sums: Technometrics, vol. 6, no. 3, p. 241-252.

DuRoss, C. B., Gold, R. D., Briggs, R. W., Delano, J. E., Ostenaa, D. A., Zellman, M. S., Cholewinski, N., Wittke, S.J., and Mahan, S. A., 2020, Holocene earthquake history and slip rate of the southern Teton fault, Wyoming, USA: GSA Bulletin, vol. 132 no. 7-8, p. 1566-1586., doi:10.1130/B35363.1.

Erener, A. and Düzgün, H.S.B., 2010, Improvement of statistical landslide susceptibility mapping by using spatial and global regression methods in the case of More and Romsdal (Norway): Landslides, vol. 7, no. 1, p. 55-68, doi:10.1007/s10346-009-0188-x.

ESRI, 2022, Add Surface Information (3D Analyst): https://pro.arcgis.com/en/pro-app/latest/tool-reference/3d-analyst/add-surface-information.htm (accessed June 2022).

ESRI, 2022, How Slope Works: https://pro.arcgis.com/en/pro-app/2.8/tool-reference/spatial-analyst/how-slope-works.htm (accessed June 2022).

ESRI, 2022, How Surface Parameters Works: https://pro.arcgis.com/en/pro-app/latest/tool-reference/spatial-analyst/how-surface-parameters-works.htm (accessed June 2022).

Ferrier, K.L., Kirchner, J.W., and Finkel, R.C., 2012, Weak influences of climate and mineral supply rates on chemical erosion rates: Measurements along two altitudinal transects in the Idaho Batholith: Journal of Geophysical Research, vol. 117, no. F2, doi:10.1029/2011JF002231.

Flannigan, M.D., Amiro, B.D., Logan, K.A., Stocks, B.J., and Wotton, B.M., 2006, Forest fires and climate change in the 21st century: Mitigation and adaptation strategies for global change, vol. 11, p. 4, p. 847-859, doi:10.1007/s11027-005-9020-7.

Foster, D., Brocklehurst, S.H., and Gawthorpe, R.L., 2010, Glacial-topographic interactions in the Teton Range, Wyoming: Journal of Geophysical Research, vol. 115, no. F01007, doi:10.1029/2008JF001135.

Galli, M., Ardizzone, F., Cardinali, M., Guzzetti, F. and Reichenbach, P., 2008, Comparing landslide inventory maps: Geomorphology, v. 94, no. 3-4, p. 268-289, doi:10.1016/j.geomorph.2006.09.023.

Goodman, L.A., 1954, Kolmogorov-Smirnov tests for psychological research: Psychological Bulletin, vol. 51, no. 2, p. 160-168, doi:10.1037/h0060275.

Gritzner, M.L., Marcus, W.A., Aspinall, R., and Custer, S.G., 2001, Assessing landslide potential using GIS, soil wetness modelingand topographic attributes, Payette River, Idaho: Geomorphology, vol. 37, no. 1-2, p. 149-165, doi: 10.1016/S0169-555X(00)00068-4.

Grohmann, C.H., Smith, M.J., and Riccomini, C., 2011, Multiscale Analysis of Topographic Surface Roughness in the Midland Valley, Scotland: IEEE Transactions on Geoscience and Remote Sensing, vol. 49, no. 4, p. 1200-1213, doi:10.1109/TGRS.2010.2053546.

Guzzetti, F., Mondini, A.C., Cardinali, M., Fiorucci, F., Santangelo, M. and Chang, K.T., 2012, Landslide inventory maps: New tools for an old problem: Earth-Science Reviews, v. 112, no. 1-2, p. 42-66, doi:10.1016/j.earscirev.2012.02.001.

Hadley, J.B., 1964, Landslides and related phenomena accompanying the Hebgen Lake earthquake of August 17, 1959: U.S. Geological Survey Professional Paper 435, p. 107-138, doi: 10.3133/pp435.

Harlan, S.S., Geissman, J.W., and Snee, L.W., 1997, Paleomagnetic and 40Ar/39Ar geochronologic data from Late Proterozoic mafic dikes and sills, Montana and Wyoming: U.S. Geological Survey Professional Paper 1580, 22 p.

Henderson, T., Santucci, V.L., Connors, T., and Tweet, J.S., 2020, National Park Service geologic type section inventory: NPS National Resource Report 2020/2198, 94 p, doi:10.36967/nrr-2283702.

Highland, L.M., 2006, Landslide Types and Processes: https://pubs.usgs.gov/fs/2004/3072/ (accessed March 2001).

Highland, L. M., and Bobrowsky, P., 2008, The landslide handbook—a guide to understanding landslides: Reston, Virginia, U.S. Geological Survey Circular 1325, 129 p, doi:10.3133/cir1325.

Hodgson, M.E., and Gaile, G.L., 1996, Characteristic mean and dispersion in surface orientations for a zone: Geographical Information Systems, vol. 10, no. 7, p. 817-830, doi:10.1080/02693799608902111.

Hong, Y., Adler, R. E., and Huffman, G. J, 2007, Satellite remote sensing for global landslide monitoring: Eos, v. 88, no. 37, p. 357– 358, doi:10.1029/2007EO370001.

Hungr, O., 2007, Dynamics of Rapid Landslides, *in* Sassa, K., Fukuoka, H., Wang, F., and G. Wang, eds, Progress in Landslide Science: Springer: Berlin, Heidelberg, Germany; New York, NY, p. 47-57.

Hungr, O., Leroueil, S., and Picarelli, L., 2014, The Varnes classification of landslide types, an update: Landslides, v. 11, no. 2, p. 167-194, doi:10.1007/s10346-013-0436-y.

Huntington, R., 2018, Cracking rock buttress finally falls above Hidden Falls: Jackson Hole News and Guide: https://www.jhnewsandguide.com/this_just_in/cracking-rock-buttress-finally-falls-above-hidden-falls/article_8969efb7-25d5-5d05-9a31-898a72f8fb64.html?msclkid=773f4dffb5cd11ec85548cff32e8bf8e (accessed April 2022).

Irigaray, C., Chacón, J., and Fernández, T., 1996, Methodology for the analysis of landslide determinant factors by means of a GIS: Application to the Colmenar area (Malaga, Spain), *in* Chacón, J., Irigaray, C., and Fernández, T., eds., Landslides: Balkema, Rotterdam, p. 163-172.

Keefer, D.K., 2000, Statistical analysis of an earthquake-induced landslide distribution — the 1989 Loma Prieta, California event: Engineering Geology, vol. 58, p. 231-249, doi:10.1016/S0013-7952(00)00037-5.

Keefer, D. K., 2002, Investigating landslides caused by earthquakes – a historical review: Surveys in Geophysics, v. 23, p. 473-510, doi:10.1023/a:1021274710840.

KellerLynn, K., 2010, Grand Teton National Park and John D. Rockefeller, Jr. Memorial Parkway: geologic resources inventory report: Natural Resource Report NPS/NRPC/GRD/ NRR—2010/230, National Park Service: Fort Collins, Colorado, 68 p.

Kim, T.K., 2017, Understanding one-way ANOVA using conceptual figures: Korean Journal of Anesthesiology, vol. 70, no. 1, p. 22-26, doi:10.4097/kjae.2017.70.1.22.

Knight, J., 2019, A new model of rock glacier dynamics: Geomorphology, vol. 340, p. 153-159, doi:10.1016/j.geomorph.2019.05.008.

Kruskal, W.H., and Wallis, W.A., 1952, Use of Ranks in One-Criterion Variance Analysis: Journal of the American Statistical Association, vol. 47, no. 260, p. 583-621.

Larsen, D.J., Crump, S.E., and Blumm, A., 2020, Alpine glacier resilience and Neoglacial fluctuations linked to Holocene snowfall trends in the western United States: Science, vol. 6., no. 47, doi:10.1126/sciadv.abc7661.

Larsen, D.J., Finkenbinder, M.S., Abbott, M.A., and Ofstun, A.R., 2016, Deglaciation and postglacial environmental changes in the Teton Mountain Range recorded at Jenny Lake, Grand Teton National Park, WY: Quaternary Science Reviews, vol. 138, p. 62-75, doi:10.1016/j.quascirev.2016.02.024.

Leopold, E.B., Liu, G., Love, J.D.; and Love, D.W., 2007, Plio-Pleistocene climatic transition and the lifting of the Teton Range, Wyoming: Quaternary Research, v. 67, p. 1-11.

Licciardi, J.M., and Pierce, K.L., 2018, History and dynamics of the Greater Yellowstone Glacial System during the last two glaciations: Quaternary Science Reviews, vol. 200, p. 1-33, doi:10.1016/j.quascirev.2018.08.027.

Love, J.D., Leopold, E.B., and Love, D.W, 1978, Eocene rocks, fossils, and geologic history, Teton Range, northwestern Wyoming: Wyoming Geological Survey Professional Paper 932-B, 55 p, doi:10.3133/pp932b.

Love, J.D., Reed Jr, J.C, and Christiansen, A.C., 1992, Geologic map of Grand Teton National Park, Teton County, Wyoming: US Geological Survey Miscellaneous Investigations Series Map I-2031: Reston, Virginia, scale 1:62,500, doi:10.3133/i2031 (digitized by National Park Service, 2010).

Love, J. D., Reed, J. C. Jr., and Pierce, K. L., 2003, Creation of the Teton landscape: A geological chronicle of Jackson Hole and the Teton Range: Grand Teton Natural History Association, Moose, Wyoming, USA, 132 p.

Marston, R. A., Weihs, B. J., and Butler, W. D., 2011, Slope failure and cross-valley profiles, Grand Teton National Park, Wyoming: University of Wyoming-National Park Service Research Center 33rd Annual Report 2010, p. 51-64, doi:10.13001/uwnpsrc.2011.3783.

MathWorks, 2022, boxplot: Visualize summary statistics with box plot: https://www.mathworks.com/help/stats/boxplot.html (accessed June 2022).

Mauch, J.P., Alexander, K.A., and Wittke, S.J., 2021, Preliminary surficial geologic map of the west half of the Jackson Lake 30' x 60' quadrangle, Teton County, Wyoming: Wyoming State Geological Survey Open File Report 2021-3, 22 p., scale 1:100,000.

McKean, J., and Roering, J., 2004, Objective landslide detection and surface morphology mapping using high-resolution airborne laser altimetry: Geomorphology, v. 57, no. 3-4, p. 331-351, doi:10.1016/s0169-555x(03)00164-8.

Minár, J., Evans, I.S., and Jenčo, M., 2020, A comprehensive system of definitions of land surface (topographic) curvatures, with implications for their application in geoscience modelling and prediction: Earth-Science Reviews, vol. 211, no. 103414, doi:10.1016/j.earscirev.2020.103414.

Mondini, A.C., Guzzetti, F., Chang, K.T., Monserrat, O., Martha, T.R., and Manconi, A., 2021, Landslide failures detection and mapping using Synthetic Aperture Radar: Past, present and future: Earth-Science Reviews, vol. 216, no. 103574, doi:10.1016/j.earscirev.2021.103574.

Moreno, M., Levachkine, S., Torres, M., and Quintero, R., 2003, Geomorphometric Analysis of Raster Image Data to Detect Terrain Ruggedness and Drainage Density, *in* Proceedings, Progress in Pattern Recognition, Speech and Image Analysis, Iberoamerican Congress on Pattern Recognition, 8th, Havana, Cuba, p. 643-650, doi:10.1007/978-3-540-24586-5_79.

Morgan, L.A., and McIntosh, W.C., 2005, Timing and development of the Heise volcanic field, Snake River Plain, Idaho, western USA: Geological Society of America Bulletin, v. 117, p. 288–301.

Napieralski, J., Barr, I., Kamp, U., Kervyn, M., 2013, Remote sensing and GIScience in geomorphological mapping, *in* Shroder, J, and Bishop, M.P., eds., Treatise on Geomorphology: Academic Press, San Diego, CA, vol. 3, p. 187-227, doi:10.1016/B978-0-12-374739-6.00050.

National Park Service (NPS), 2019, Park statistics, Grand Teton National Park, https://www.nps.gov/grte/learn/management/statistics.htm (accessed February 2021).

Nefeslioglu, H.A., Duman, T.Y., and Durmaz, S., 2008, Landslide susceptibility mapping for a part of tectonic Kelkit Valley (Eastern Black Sea region of Turkey): Geomorphology, vol. 94, no. 3-4, p. 401-418, doi:10.1016/j.geomorph.2006.10.036.

Nicholas, G.E., 2018, Landslide Morphology and its Insight into the Timing and Causes of Slope Failure: Case Study of Post-Glacial Landslides in Yellowstone National Park [MS thesis]: Bozeman, Montana State University, 61 p.

Palacios-González, F., and García-Fernández, R.M., 2012, Interpretation of the coefficient of determination of an ANOVA model as a measure of polarization: Journal of Applied Statistics, vol. 39, no. 7, p. 1543-1555, doi:10.1080/02664763.2012.658361.

Pánek, T., Břežný, M., Kapustová, V., Lenart, J., and Chalupa, V., 2019, Large landslides and deep-seated gravitational slope deformations in the Czech Flysch Carpathians: New LiDAR-based inventory: Geomorphology, vol. 346, no. 106852, doi:10.1016/j.geomorph.2019.106852.

Pellicani, R., Frattini, P., and Spilotro, G., 2014, Landslide susceptibility assessment in Apulian Southern Apennine: heuristic vs. statistical methods: Environmental earth sciences, vol. 72, no. 4, p. 1097-1108, doi:10.1007/s12665-013-3026-3.

Pierce, K.L, Licciardi, J.M., Good, J.M., and Jaworowski, C., 2018, Pleistocene glaciation of the Jackson Hole area, Wyoming: U.S. Geological Survey Professional Paper 1835, 56 p., doi:10.3133/pp1835.

Regmi, N.R., and Walter, J.I., 2020, Detailed mapping of shallow landslides in eastern Oklahoma and western Arkansas and potential triggering by Oklahoma earthquakes: Geomorphology, vol. 366, no. 106806, p. 9, doi:10.1016/j.geomorph.2019.05.026.

Regmi, N.R., McDonald, E.V., and Bacon, S.N., 2013, Mapping Quaternary alluvial fans in the southwestern United States based on multiparameter surface roughness of lidar topographic data: JGR Earth Surface, vol. 119, no. 1, p. 12-27, doi:10.1002/2012JF002711.

Reichenbach, P., Rossi, M., Malamud, B.D., Mihir, M. and Guzzetti, F., 2018, A review of statistically-based landslide susceptibility models: Earth-science reviews, vol. 180, p. 60-91, doi:10.1016/j.earscirev.2018.03.001.

Rivera, T.A., Schmitz, M.D., Crowley, J.L., and Storey, M., 2014, Rapid magma evolution constrained by zircon petrochronology and 40Ar/39Ar sanidine ages for the Huckleberry Ridge Tuff, Yellowstone, USA: Geology, vol. 42, no. 8, p.643-646, doi:10.1130/G35808.1.

Rogerson, P., 2015, Spatial Statistical Methods for Geography (fourth edition): London, UK, SAGE Publications, 256 p.

Sahin, E.K., Ipbuker, C., Kavzoglu, T., 2017, Investigation of automatic feature weighting methods (Fisher, Chi-square and Relief-F) for landslide susceptibility mapping: Geocarto International, vol. 32, no. 9, p. 956-977, doi:10.1080/10106049.2016.1170892.

Shamloo, H.I., and Till, C.B., 2019, Decadal transition from quiescence to supereruption: petrologic investigation of the Lava Creek Tuff, Yellowstone Caldera, WY: Contributions to Mineralogy and Petrology, vol. 174, no. 32, 18 p., doi:10.1007/s00410-019-1570-x.

Shi, X., Zhu., A.X., Burt, J., Choi, W., Wang, R., Pei, T., Li., B., and Qin, C., 2007, An Experiment Using a Circular Neighborhood to Calculate Slope Gradient from a DEM: Photogrammetric Engineering & Remote Sensing, vol. 73, no. 2, p. 143-154, doi:10.14358/PERS.73.2.143.

Shroder, J., and Weihs, B., 2014, Mass movement disturbance regime landscapes, hazards, and water implications: Grand Teton National Park, Wyoming: University of Wyoming-National Park Service Research Center 36th Annual Report, 4-2014, 16 p., doi:10.13001/uwnpsrc.2013.3987.

Slaughter, S.L., Burns, W.J., Mickelson, K.A., Jacobacci, K.E., Biel, A., and Contreras, T.A., 2017, Protocol for Landslide Inventory Mapping from LiDAR Data in Washington State: Washington Geological Survey Bulletin 82, 27 p.

Smedes, H. W., and Prostka, H. J., 1972, Stratigraphic framework of the Absaroka Volcanic Supergroup in the Yellowstone National Park region: U.S. Geological Survey Professional Paper 729-C, 32 p., doi:10.3133/pp729C.

Smith, R.B., Byrd, J.O.D., and Susong, D.D., 1993, Seismotectonics, Quaternary history, and earthquake hazards of the Teton fault, Wyoming, *in* Snoke, A., Steidmann, J.R., and Roberts, S., eds., Geology of Wyoming: Geological Society of Wyoming, Laramie, Memoir no. 5, p. 628-667.

Soeters, R., and van Westen, C.J., 1995, Slope instability recognition, analysis, and zonation, *in* Turner, A.K., and Schuster, R.L., eds., Landslides, investigation and mitigation: Transportation Research Board Special Report 247: Washington, D.C., National Research Council, p. 129-177.

Stevenson, P.C., 1977, An empirical method for the evaluation of relative landslip risk: Bulletin of the International Association of Engineering Geology, vol. 16, p. 69–72, doi:10.1007/BF02591451.

Suzen, M.L., and Doyuran, V., 2004, Data driven bivariate landslide susceptibility assessment using geographical information systems: a method and application to Asarsuyu catchments, Turkey: Engineering Geology, vol. 71, no. 3-4, p. 303–321, doi:10.1016/s0013-7952(03)00143-1.

Syrjala, S., 1996, A Statistical Test for a Difference between the Spatial Distributions of Two Populations: Ecology, vol. 77, no. 1, p. 75-80, doi:10.2307/2265656.

Tranel, L.M., and Strow, M.L., 2017, 10Be analysis of amalgamated talus pebbles to investigate alpine erosion, Garnet Canyon, Teton Range, Wyoming: Geosphere, v. 13, no. 1, p. 36–48, doi:10.1130/GES01297.1.

van Westen, C. J., 1993, Application of geographic information systems to landslide hazard zonation [Ph.D. thesis]: Enschede, The Netherlands, University of Twente, 286 p.

van Westen, C. J., 2013, Remote sensing and GIS for natural hazards assessment and disaster risk management, *in* Shroder, J, and Bishop, M.P., eds., Treatise on Geomorphology: Academic Press, San Diego, CA, vol. 3, p. 259-298, doi:10.1016/B978-0-12-374739-6.00051-8.

Vandromme, R., Thiery, Y., Bernardie, S., and Sedan, O., 2020, ALICE (Assessment of landslides induced by climatic events): A single tool to integrate shallow and deep landslides for susceptibility and hazard assessment: Geomorphology, v. 367, no. 107307, doi:10.1016/j.geomorph.2020.107307.

Varnes, D.J., 1978, Slope movement types and processes, in Schuster, R.L., and Krizek, R.J., eds., Landslides, analysis and control: Transportation Research Board Special Report 176: Washington, DC., National Academy of Sciences, p. 11–33.

White, B. J. P., Smith, R. B., Husen, S., Farrell, J. M., and I. Wong, 2009. Seismicity and earthquake hazard analysis of the Teton-Yellowstone region, Wyoming: Journal of Volcanology and Geothermal Research, v. 188, p. 277–296.

Woolpert, 2014, Grand Teton National Park and National Elk Refuge-LiDAR acquisition: https://woolpert.com/project/grand-teton-national-park-and-national-elk-refuge-lidar-acquisition (accessed June 2022).

Zartman, R.E., and Reed Jr, J.C., 1998, Zircon geochronology of the Webb Canyon gneiss and the Mount Owen quartz monzonite, Teton Range, Wyoming: Significance to dating late Archean metamorphism in the Wyoming Craton: The Mountain Geologist, vol. 35, no. 2, p. 71-77.

Zellman, M.S., DuRoss, C.B., and Thackray, G.D., 2019, The Teton fault—Teton County, Wyoming: Wyoming State Geological Survey Open File Report 2019-1, scale 1:75,000.

Appendix 1: Results of Shapiro-Wilk and Levene's Tests

Table A1.1: p-values reported from the Shapiro-Wilk test of normality in which the distribution of each movement style was assessed for each of the topographic variables. Small p-values cast doubt on the null hypothesis that a given movement style is normally distributed within a given topographic variable.

Variable Compared	p-value			
	Debris Flows	Rockfall/Topple	Earth Flows	Slides
Slope	5.99E-07	1.72E-05	6.00E-03	2.12E-12
Aspect	1.71E-09	4.82E-07	2.00E-10	2.87E-05
Local Vertical Relief	1.80E-03	0.285	9.46E-12	4.97E-08
Plan Curvature	3.84E-06	3.02E-06	2.73E-07	5.54E-07
Profile Curvature	<0.000005	5.61E-11	5.32E-06	9.40E-07
Topographic Roughness	7.77E-16	8.24E-05	4.58E-10	5.29E-13

Table A1.2: p-values reported from Levene's test of equal variance in which the of the distribution of each movement style was compared across each of the topographic variables. The small p-values cast doubt on the null hypothesis that the movement styles' variances are equal across a given topographic variable.

Variable Compared	p-value
Slope	3.23E-18
Aspect	2.80E-07
Local Vertical Relief	1.39E-10
Plan Curvature	6.90E-75
Profile Curvature	2.03E-31
Topographic Roughness	7.11E-43

Appendix 2: Results of Average Nearest Neighbor Test

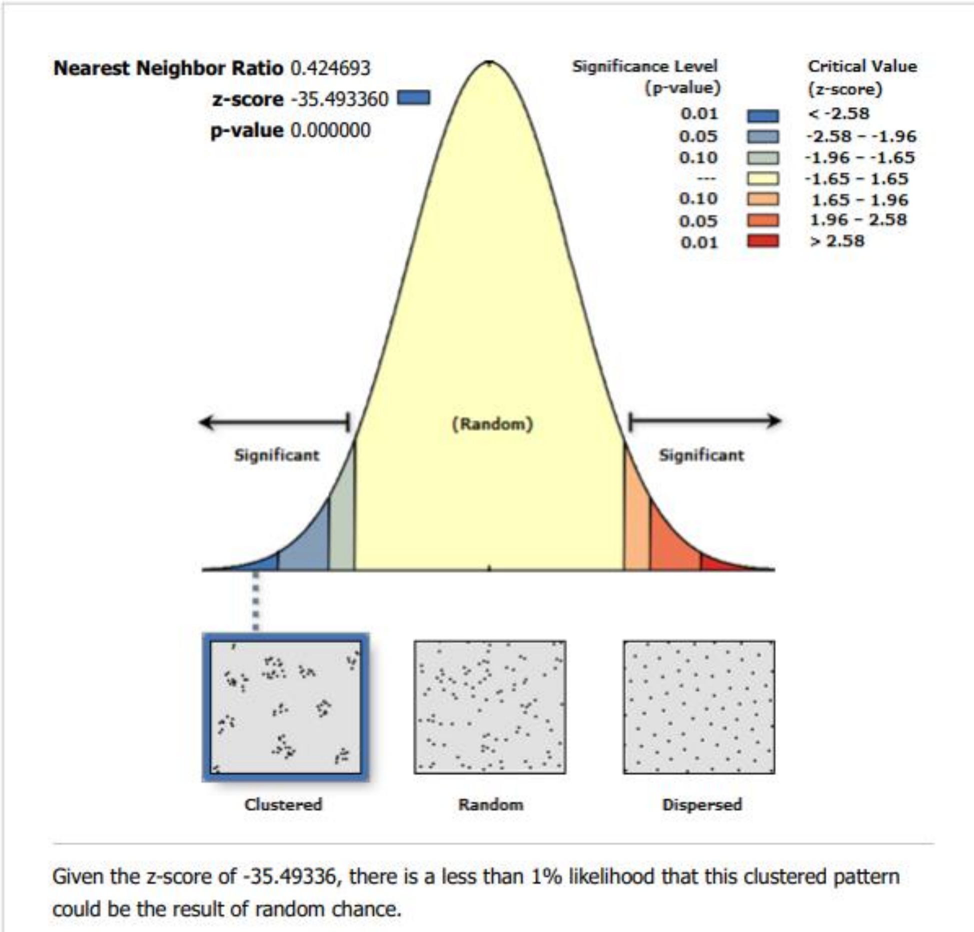

Average Nearest Neighbor Summary

Observed Mean Distance	344.9897 Meters
Expected Mean Distance	812.3271 Meters
Nearest Neighbor Ratio	0.424693
z-score	-35.493360
p-value	0.000000

Figure A2.1: Report generated from the average nearest neighbor test in which the average distance between movements was compared with the distance expected if all movements were randomly distributed across the study area. The test identified a strong clustering pattern, suggesting that movements initiate in unique locations within GTNP.

Appendix 3: Results of Syrjala’s Test

Table A3.1: p-values reported from Syrjala’s test of spatial independence between populations in which pairwise comparisons were made between the kernel density distributions of each movement style. Small p-values support the alternative hypothesis that the normalized spatial distributions of the compared movement styles vary across GTNP.

Group	Control Group	p-value
Debris Flow	Earth Flow	<0.000005
Debris Flow	Fall/Topple	<0.000005
Debris Flow	Slide	<0.000005
Earth Flow	Fall/Topple	<0.000005
Earth Flow	Slide	<0.000005
Fall/Topple	Slide	<0.000005

Appendix 4: Results of Two-sample Kolmogorov-Smirnov Test

Table A4.1: p-values reported from the Two-sample Kolmogorov-Smirnov Test in which the distribution of each variable was compared to that of the bulk study area. Small p-values support the alternative hypothesis that that attribute of landslide-producing topography is different from that of the bulk study area.

Variable Compared	**p-value**
Slope	1.53E-202
Aspect	0.0019
Local Vertical Relief	1.16E-48
Plan Curvature	1.21E-58
Profile Curvature	9.41E-04
Topographic Roughness	2.54E-68

Appendix 5: Results of Kruskal-Wallis and Dunn's Tests

Table A5.1: p-values reported from the Kruskal-Wallis test in which the distribution of each movement style was compared for each of the topographic variables. Small p-values support the alternative hypothesis that at least one of the movement styles originated from a separate population based on that variable. The coefficient of determination (R^2) describes the percentage of the total variance within each variable that can be explained by separate populations.

Variable Compared	p-value	R^2
Slope	2.57E-148	0.660
Aspect	0.1562	0.005
Local Vertical Relief	3.88E-110	0.491
Plan Curvature	7.34E-83	0.369
Profile Curvature	9.83E-19	0.084
Topographic Roughness	8.48E-82	0.365

Table A5.2: p-values reported from Dunn's Test in which pairwise comparisons were made between all movement styles on the basis of their slope. Small p-values support the alternative hypothesis that the compared movement styles can be differentiated by their slope.

Group	Control Group	p-value
Debris Flow	Earth Flow	3.77E-09
Debris Flow	Fall/Topple	3.77E-09
Debris Flow	Slide	3.77E-09
Earth Flow	Fall/Topple	3.77E-09
Earth Flow	Slide	0.0012273
Fall/Topple	Slide	3.77E-09

Table A5.3: p-values reported from Dunn's Test in which pairwise comparisons were made between all movement styles on the basis of their vertical relief. Small p-values support the alternative hypothesis that the compared movement styles can be differentiated by their vertical relief.

Group	Control Group	p-value
Debris Flow	Earth Flow	<0.00005
Debris Flow	Fall/Topple	0.24238
Debris Flow	Slide	<0.00005
Earth Flow	Fall/Topple	<0.00005
Earth Flow	Slide	0.018093
Fall/Topple	Slide	<0.00005

Table A5.4: p-values reported from Dunn's Test in which pairwise comparisons were made between all movement styles on the basis of their topographic surface roughness. Small p-values support the alternative hypothesis that the compared movement styles can be differentiated by their surface roughness.

Group	Control Group	p-value
Debris Flow	Earth Flow	3.77E-09
Debris Flow	Fall/Topple	3.79E-09
Debris Flow	Slide	3.77E-09
Earth Flow	Fall/Topple	3.77E-09
Earth Flow	Slide	0.6650877
Fall/Topple	Slide	3.77E-09

Table A5.5: p-values reported from Dunn's Test in which pairwise comparisons were made between all movement styles on the basis of their plan curvature. Small p-values support the alternative hypothesis that the compared movement styles can be differentiated by their plan curvature.

Group	Control Group	p-value
Debris Flow	Earth Flow	3.77E-09
Debris Flow	Fall/Topple	3.77E-09
Debris Flow	Slide	3.77E-09
Earth Flow	Fall/Topple	0.6085313
Earth Flow	Slide	0.976152
Fall/Topple	Slide	0.9056039

Table A5.6: p-values reported from Dunn's Test in which pairwise comparisons were made between all movement styles on the basis of their profile curvature. Small p-values support the alternative hypothesis that the compared movement styles can be differentiated by their profile curvature.

Group	Control Group	p-value
Debris Flow	Earth Flow	0.0010831
Debris Flow	Fall/Topple	3.77E-09
Debris Flow	Slide	0.011162
Earth Flow	Fall/Topple	8.97E-07
Earth Flow	Slide	1
Fall/Topple	Slide	2.82E-05

Appendix 6: Results of Chi-Square Test

Table A6.1: p-values reported from the Chi-Square Test in which the distribution of substrate lithologies within each mass movement style was compared to that of all mass movements. The lithology distribution of all mass movements was also compared to that of the bulk study area. Small p-values suggest that the four mass movement styles occur in unique lithological settings and that the distribution of landslide-producing lithologies does not reflect the distribution of those contained within the bulk study area.

Groups Compared	**p-value**
Debris Flows to all movements	7.98E-39
Slides to all movements	1.33E-26
Rockfall/Topple to all movements	5.23E-07
Earth Flows to all movements	6.37E-52
All movements to bulk field area	1.48E-224

Table A6.2: Observed and expected counts of debris flow substrate lithologies used as inputs for the chi-square test. The expected counts are proportional to the overall substrate distribution among all movement styles.

Dominant Substrate Lithology	**Actual Count**	**Actual Count (%)**	**Expected Count**	**Expected Count (%)**
Extrusive	20	4.4%	64	14.0%
Intrusive and Metamorphic	378	83.1%	235	51.7%
Sedimentary	48	10.5%	127	27.9%
Surficial Deposits	9	2.0%	29	6.3%
Grand Total	**455**	**100.00%**	**455**	**100.00%**

Table A6.3: Observed and expected counts of rockfall/topple substrate lithologies used as inputs for the chi-square test. The expected counts are proportional to the overall substrate distribution among all movement styles.

Dominant Substrate Lithology	**Actual Count**	**Actual Count (%)**	**Expected Count**	**Expected Count (%)**
Extrusive	12	6.3%	27	14.0%
Intrusive and Metamorphic	132	68.8%	99	51.7%
Sedimentary	48	25.0%	54	27.9%
Surficial Deposits	0	0.0%	12	6.3%
Grand Total	**192**	**100.00%**	**192**	**100.00%**

Table A6.4: Observed and expected counts of <u>earth flow</u> substrate lithologies used as inputs for the chi-square test. The expected counts are proportional to the overall substrate distribution among all movement styles.

Dominant Substrate Lithology	Actual Count	Actual Count (%)	Expected Count	Expected Count (%)
Extrusive	64	25.7%	35	14.0%
Intrusive and Metamorphic	14	5.6%	129	51.7%
Sedimentary	120	48.2%	69	27.9%
Surficial Deposits	51	20.5%	16	6.3%
Grand Total	**249**	**100.00%**	**249**	**100.00%**

Table A6.5: Observed and expected counts of <u>slide</u> substrate lithologies used as inputs for the chi-square test. The expected counts are proportional to the overall substrate distribution among all movement styles.

Dominant Substrate Lithology	Actual Count	Actual Count (%)	Expected Count	Expected Count (%)
Extrusive	50	34.7%	20	14.0%
Intrusive and Metamorphic	14	9.7%	74	51.7%
Sedimentary	74	51.4%	40	27.9%
Surficial Deposits	6	4.2%	9	6.3%
Grand Total	**144**	**100.00%**	**144**	**100.00%**

Table A6.6: Observed and expected counts of <u>mass movement</u> substrate lithologies used as inputs for the chi-square test. The expected counts are proportional to the overall distribution of lithologies throughout the bulk study area.

Dominant Substrate Lithology	Actual Count	Actual Count (%)	Expected Count	Expected Count (%)
Extrusive	146	14.0%	89	8.6%
Intrusive and Metamorphic	538	51.7%	228	21.9%
Sedimentary	290	27.9%	150	14.4%
Surficial Deposits	66	6.3%	573	55.1%
Grand Total	**1040**	**100.00%**	**1040**	**100.00%**